JGR Oceans

RESEARCH ARTICLE
10.1029/2018JC014682

Special Section:
The U.S IOOS Coastal and Ocean Modeling Testbed 2013-2017

Baroclinic Coupling Improves Depth-Integrated Modeling of Coastal Sea Level Variations Around Puerto Rico and the U.S. Virgin Islands

William J. Pringle[1], Juan Gonzalez-Lopez[2], Brian R. Joyce[1], Joannes J. Westerink[1], and Andre J. van der Westhuysen[3]

[1]Department of Civil and Environmental Engineering and Earth Sciences, University of Notre Dame, Notre Dame, IN, USA, [2]Wood, E&IS, Met-Ocean Services, Dartmouth, NS, Canada, [3]IMSG at NOAA/NWS/NCEP/Environmental Modeling Center, 5830 University Research Court, College Park, MD, USA

Abstract This study applies a baroclinic-coupled depth-integrated modeling system to the North Atlantic Ocean, where an unstructured mesh is used to focus resolution down to ~30 m along the coasts of Puerto Rico and the U.S. Virgin Islands. Ocean baroclinicity is incorporated through one-way coupling from operational data-assimilated Global Ocean Forecasting System 3.1 temperature and salinity fields at just 12% additional computational time. The main objectives are to provide a comprehensive analysis of observed and modeled coastal sea levels (spanning from seasonal to supertidal variations) in Puerto Rico and the U.S. Virgin Islands during 2017 and to evaluate the associated model performance with and without baroclinic coupling at 14 National Oceanic and Atmospheric Administration/National Ocean Service tide gauges deployed in the region. It is found that baroclinic coupling increases modeled energy across the entire frequency spectrum, which is more commensurate with observations. In particular, density-driven effects such as the seasonal cycle and sea level setdown due to trailing cold wakes from passing hurricanes are largely reproduced. Supertidal shelf-resonant seiching at one to two cycles per hour is observed and modeled at a number of locations, where excitation of these modes is often promoted by the baroclinic coupling. Baroclinicity improves the yearlong model skill at every tide gauge, where the mean total skill is increased from 87% to 93% accuracy (54% to 85% for the nontidal residual). In September 2017 during Hurricanes Irma and Maria, baroclinicity increases model skill at 10 out of 14 tide gauges even when the barotropic mode is adjusted to have no mean offset from the observations.

Plain Language Summary Computer simulations (models) with fine scales at the coast are required to accurately forecast coastal water levels potentially causing flooding. Often these computer models only account for the effects of winds and air pressure (creating surge), and gravity from the Moon and the Sun (creating tides), ignoring the effects of ocean density because of the large computational expense required. In this study we present an approach to incorporate ocean density effects into the fine-scale model by using information from an existing coarse-scaled ocean model already in operation. This results in a small and manageable 12% increase to computational run-times. The approach is assessed by comparing model results to measured coastal sea levels during 2017 around Puerto Rico and the U.S. Virgin Islands. It is found that a range of density-induced variations in coastal sea levels could be reproduced such as those related to seasonal heating-cooling cycles, and temporary cooling of the local ocean surface due to 2017 Hurricanes Maria and Irma. Measures of model accuracy show that the inclusion of ocean density leads to improvements in the simulation of yearly coastal water levels at every location tested. Based on the positive results this approach may be useful for improving existing operational forecast computer simulations.

Key Points:
- Ocean baroclinicity is incorporated into a high-resolution depth-integrated coastal ocean model at just 12% additional computational time
- Density-driven impacts to coastal sea levels are accurately captured (e.g., seasonal cycle and hurricane-induced upwelling causing setdown)
- Yearlong assessment of regional coastal sea levels during 2017 shows that baroclinic coupling consistently improves model skill

Supporting Information:
- Supporting Information S1
- Data Set S1
- Table S1

Correspondence to:
W. J. Pringle,
wpringle@nd.edu

Citation:
Pringle, W. J., Gonzalez-Lopez, J., Joyce, B. R., Westerink, J. J., & van der Westhuysen, A. J. (2019). Baroclinic coupling improves depth-integrated modeling of coastal sea level variations around Puerto Rico and the U.S. Virgin Islands. *Journal of Geophysical Research: Oceans*, *124*, 2196–2217. https://doi.org/10.1029/2018JC014682

Received 18 OCT 2018
Accepted 8 FEB 2019
Accepted article online 13 FEB 2019
Published online 29 MAR 2019

1. Introduction

Operational forecasts of coastal sea level and flooding is a vital part of the U.S. Integrated Ocean Observing System (IOOS) program. Previous research efforts to better understand storm-induced flooding targeted mild-sloped U.S. mainland environments (e.g., Bunya et al., 2010; Hope et al., 2013; Kerr, Donahue,

et al.,2013; Kerr, Martyr, et al.,2013; Orton et al., 2012; Westerink et al., 2008; Zheng et al., 2013). However, a recent focus has been on Puerto Rico and the U.S. Virgin Islands (PRVI) where a large number of observational instruments have been deployed as part of the Caribbean Coastal Ocean Observing System. The PRVI region is a steep-sloped narrow shelf island environment, located on an underwater mountain range between the Caribbean Sea and the Atlantic Ocean, which frequently experiences tropical storms and hurricanes during the months of August and September (https://www.nhc.noaa.gov/climo/). Recently in September 2017, two Category 5 hurricanes, Irma and Maria, severely impacted the Caribbean region in quick succession resulting in high waves, storm tide, and river flooding causing widespread damage (Cangialosi et al., 2018; Pasch et al., 2018).

In the light of these recent multibillion dollar damaging hurricane events, combined with the threat of future sea level rise, it is timely and relevant to thoroughly examine the state-of-the-art in storm tide modeling for PRVI and similar deep ocean islands as part of the U.S. IOOS funded Coastal and Ocean Modeling Testbed (Luettich et al., 2017). In particular, this study conducts a detailed analysis of a high-resolution depth-integrated coastal ocean modeling system in terms of its ability to capture the entire frequency spectrum of 6-min coastal sea level variations around PRVI compared to tide gauges observations during 2017. Simultaneously, a coupling technique that allows for the effects of ocean baroclinicity to be accounted for in the depth-integrated model is investigated. In addition to advancing our understanding of the coastal processes around PRVI and steep-sloped island regions in general, the results of this study can be used to improve operational forecast models and future estimates of coastal flooding risk taking into account the dynamic effects of ocean warming, ice melt, and changing ocean current systems on sea levels. Note that the effects of wind waves are ignored here. A companion paper featured in this special issue (Joyce et al., 2019) is concerned with the analysis of the relative contributions of wind waves and surge in a two-way coupled modeling system around PRVI.

The ADvanced CIRCulation (ADCIRC) finite-element coastal ocean model (Luettich & Westerink, 2004) is used to provide operational forecast guidance of storm tide along U.S. coastlines. For impending Atlantic Ocean hurricane events the ADCIRC Surge Guidance System (Fleming et al., 2008; https://cera. coastalrisk.live/) and the U.S. National Oceanic and Atmospheric Administration (NOAA) Hurricane Surge On-demand Forecast System (Vinogradov et al., 2017) are used. For continuous year-round forecasting of extratropical events the NOAA Extratropical Surge and Tide Operational Forecast System (Funakoshi et al., 2011; https://ocean.weather.gov/estofs/estofs_surge_info.shtml), covering both the Pacific Ocean and the Atlantic Ocean coastlines with two separate models is used. Thus, ADCIRC was chosen to be a part of the IOOS Coastal and Ocean Modeling Testbed project which aims to thoroughly assess model performance to understand and recommend how new model developments can be transitioned into such operational forecast models. ADCIRC employs unstructured triangular meshes to accurately conform to complex geometries and topographic features by providing locally high mesh refinement, while covering a large area of interest with relatively few mesh elements by using comparatively coarse resolution away from the coastline and important topographic features (e.g., Technology Riverside Inc & AECOM, 2015; Westerink et al., 2008). Although ADCIRC has a three-dimensional baroclinic mode (3D-BC), it is predominantly used in two-dimensional depth-integrated barotropic mode (2DDI-BT). This is because ADCIRC is often used to model tides and surge on the inner shelf and adjacent coastal floodplain. Tides and surge are described by long waves that develop due to external astronomical (gravitational attraction) and meteorological forces (surface wind stresses and atmospheric pressure). Usually internal ocean dynamics are considered to be of relatively small significance to the external dynamics of tides and surge. On the other hand, ADCIRC is typically coupled to nonphase resolving wind wave models to account for the interaction between ordinary gravity waves and short wave portions of the spectrum which can result in wave-induced setup and alongshore currents at the coast (e.g., Dietrich et al., 2011).

The islands in the PRVI region are surrounded by narrow continental shelves and steep shelf breaks. Since surge over wide and shallow continental shelves is larger than over steep offshore slopes (Resio & Westerink, 2008) and tidal amplitudes are relatively small in the Caribbean region (Kjerfve, 1981), wind wave setup and run-up makes up a large relative contribution to extreme water levels and coastal flooding throughout PRVI (Melet et al., 2018), as in other steep-sloped island regions, for example, Hawaii (Kennedy et al., 2012). Nevertheless, it is important to correctly simulate circulation processes related to tide, surge, subtidal, and supertidal coastal sea level variations because it is the combination of all these physical processes that ultimately makes up the total coastal sea level and hence the flooding risk. Furthermore, circulation processes

affect the propagation of waves and the location of wave-breaking zones in the coastal zone (Dietrich et al., 2011). The 2DDI-BT models can simulate a large proportion of such coastal sea level variations by accounting for the barotropic response to astronomical and meteorological forcing (Carrére & Lyard, 2003). Also, while yet to be implemented into operational forecasting, 2DDI-BT ADCIRC models have been coupled to hydrological models to account for rainfall and river flooding effects in a number of studies (Bacopoulos et al., 2017; Dresback et al., 2013; Van Cooten et al., 2011), including most recently in PRVI (Silva-Araya et al., 2018). However, the effects of seasonal warming and cooling cycles, baroclinically driven ocean currents, upwelling events, and fresh-saline water interactions cannot be accounted for. The impacts of these can be significant, for example, the seasonal sea level cycle can account for a significant proportion (up to 78%) of the coastal sea level variability in the Caribbean (Torres & Tsimplis, 2012). Thus, 2DDI-BT ADCIRC cannot completely fulfill the needs of operational forecasting systems for the PRVI region.

This study seeks to investigate a baroclinic-coupled 2DDI (2DDI-BC) mode version of ADCIRC for the purposes of advancing operational (usually 2DDI) storm tide forecast models, and coastal ocean modeling of sea level variations and circulation in general. To achieve baroclinic coupling, an operational data-assimilated 3D-BC global ocean model is used to provide the vertical density and current structure of the ocean. The idea is that although 2DDI models cannot directly simulate oceanographic processes they *can* account for their effects to the free surface and depth-integrated currents. This could be seen as being similar to explicit mode-splitting schemes between external and internal modes used in ocean models (e.g., Shchepetkin & McWilliams, 2005), however here we only weakly couple one-way from the internal mode to the external mode, resetting the density and current structure as new data from the 3D-BC model is available. Thus, the internal and external modes are heterogeneous and operate at widely disparate spatial and temporal scales. Since modern 3D-BC global oceans are now of sufficient resolution (for modeling the ocean but not the coast) and so well constrained through complex data-assimilated networks, making use of this high value-low cost information may help 2DDI models overcome their limitations.

In this study, the operational Global Ocean Forecast System (GOFS 3.1; Metzger et al., 2017)—an operation data-assimilated (Cummings, 2006) 1/12° global implementation of the HYbrid Coordinate Ocean Model (HYCOM; Chassignet et al., 2007)—is chosen to be one-way coupled to 2DDI-BC ADCIRC. GOFS 3.1 provides oceanographic outputs every 3 hr. The main coupling procedure involves using GOFS 3.1 temperature and salinity fields to compute depth-integrated baroclinic pressure gradients which are interpolated onto the 2DDI-BC mesh, driving large-scale baroclinic-related sea level variations in the 2DDI-BC model. Further, the vertical current structure of GOFS 3.1 is used to compute momentum dispersion, and the effects of oceanic processes that develop outside of the 2DDI-BC computational domain are propagated in through lateral open boundary conditions specifying the GOFS 3.1 free surface. Finally, the 2DDI-BC model parameterizes the effect of energy conversion from barotropic tides to baroclinic internal tides in deep water (e.g., Egbert et al., 2004; Green & Nycander, 2013; Pringle, Wirasaet, Suhardjo, et al., 2018; Pringle, Wirasaet, & Westerink, 2018; Wilmes et al., 2017), which is a function of ocean buoyancy computed from the GOFS 3.1 temperature and salinity fields.

This paper is organized as follows. Section 2 begins by outlining the computational mesh domain, the 2DDI ADCIRC numerical model, simulation setup and computational times, and the data sources used such as bathymetry and tide gauge observations. This is followed by the results (section 3) which are split into two sections: Section 3.1 presents an analysis of the characteristics of the observed and modeled coastal sea levels (divided into tidal, seasonal, local subtidal and surge, and supertidal components) and how they compare; and section 3.2 evaluates model errors and skill against tide gauge observations for all of 2017 and for just September 2017. Finally, the results are discussed and prospects for future work related to the 2DDI-BC model are outlined (section 4).

2. Computational Mesh Domain, Methods, and Data Sources

2.1. Computational Mesh Domain

The computational mesh domain covers the North Atlantic Ocean (Figure 1). Overland regions are excluded. The mesh is generated objectively, reproducibly, and automatically using the state-of-the-art MATLAB toolbox, OceanMesh2D 1.0 (Roberts et al., 2018). The toolbox applies a set of mesh size functions requiring user-defined parameters to vary resolution according to geometric and topographic considerations. All parameters and data sources used to generate the mesh are described in Data Set S1, which is a MATLAB

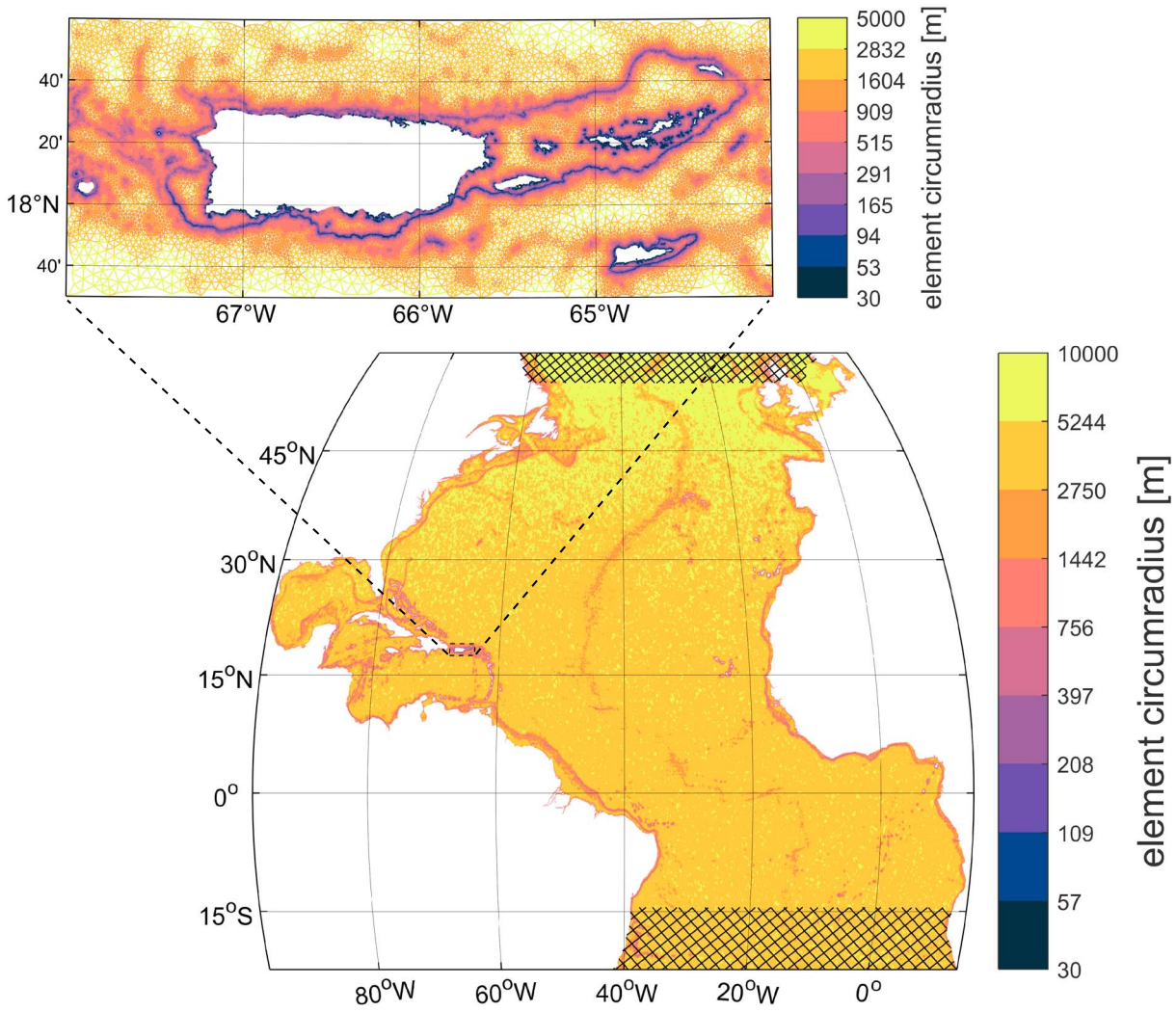

Figure 1. Computational unstructured triangular mesh domain with the colors indicating the local mesh resolution (defined as the element circumradius), which reaches ~5–10 km in the deep ocean and becomes as small as ~30 m along the coast and shelf break regions of Puerto Rico and the U.S. Virgin Islands (upper left inset). The hatched region indicates the location of the absorption-generation sponge layer that is applied in the vicinity of the lateral open boundaries.

script that can be used with OceanMesh2D to reproduce the mesh, in addition to ADCIRC input files necessary for simulation. The total number of mesh vertices is 1.5 million, with 0.22 million vertices concentrated in the PRVI region (upper left inset in Figure 1). Higher resolution is automatically placed in regions of large topographic gradient (e.g., continental shelf breaks) and along geometrically complex and constricted coastlines. Compared to unstructured meshes built by hand in the past (e.g., Joyce et al., 2019), resolution is highly targeted resulting in fewer vertices despite high resolution (~30 m) in coastal areas.

Outside of the PRVI region the mesh resolution is set to a maximum of 10 km in the deep ocean and a minimum of 1 km at the coast. The high-resolution GSHHS shoreline (Wessel & Smith, 1996) is used to define the coastline, and bathymetry is interpolated from the global SRTM15_PLUS 15-arc second product (available from ftp://topex.ucsd.edu/pub/srtm15_plus/). Within the PRVI region the minimum resolution is set to 30 m. Here, the shoreline and bathymetric depths (Figure 2) are obtained from two 1-arc second NOAA NCEI digital elevation models that encompass the region, and a 1/9-arc second NOAA NCEI digital elevation models for San Juan Bay (see https://maps.ngdc.noaa.gov/viewers/bathymetry/?layers=dem). A cell-averaged technique built into the OceanMesh2D toolbox is used to interpolate bathymetric depths onto the mesh.

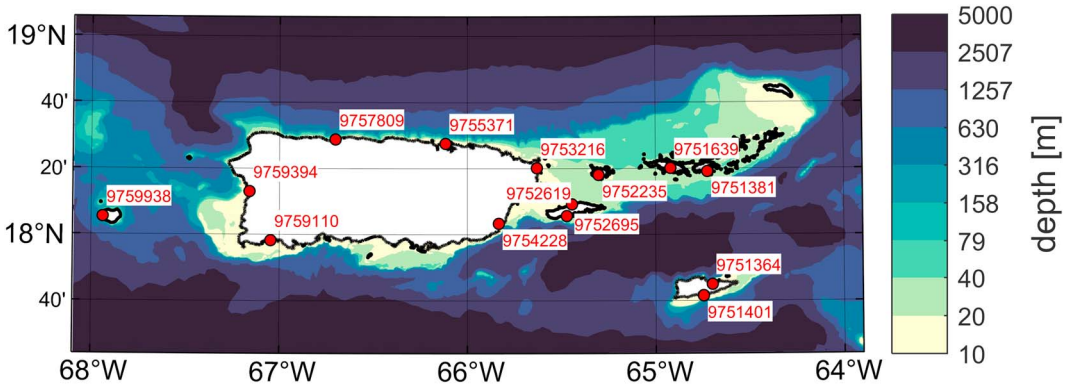

Figure 2. Bathymetric depths around the Puerto Rico and U.S. Virgin Islands region. Positions and Station IDs of the 14 National Oceanic and Atmospheric Administration/National Ocean Service tide gauges that were in operation during 2017 are indicated.

Note that the large domain extent is important for the 2DDI-BC model since lateral open boundary conditions involving 3D-BC processes that are compatible with the model become rather difficult to correctly define (in comparison to, e.g., barotropic tidal solutions). Thus, we have found that allowing the internal dynamics to have maximum control on the solution with little reliance on the lateral open boundary conditions leads to solutions with minimal spurious modes.

2.2. The 2DDI-BC Coupled ADCIRC Modeling System

The 2DDI ADCIRC finite-element model (Luettich & Westerink, 2004) is governed by the shallow water equations. Including the effects of external astronomical and meteorological forcings, internal oceanographic forcings, and terms associated with an absorptive-generative sponge layer for lateral open boundary conditions, they can be written as

$$\frac{\partial \zeta}{\partial t} + \nabla \cdot (\boldsymbol{U}H) = -\sigma(\boldsymbol{x})(\zeta - \zeta_c) \tag{1}$$

$$\begin{aligned}\frac{\partial \boldsymbol{U}}{\partial t} + \boldsymbol{U} \cdot \nabla \boldsymbol{U} + f\mathbf{k} \times \boldsymbol{U} = -\nabla \left[\frac{p_s}{\rho_0} + g(\zeta - \zeta_{EQ} - \zeta_{SAL})\right] \\ + \frac{\nabla M}{H} - \frac{\nabla D}{H} - \frac{\nabla B}{H} + \frac{\boldsymbol{\tau}_s - \boldsymbol{\tau}_b}{\rho_0 H} - C - \sigma(\boldsymbol{x})(\boldsymbol{U} - \boldsymbol{U}_c),\end{aligned} \tag{2}$$

where ζ is the free surface elevation (water elevation or sea level); $H = h + \zeta$ is the total water depth, in which h is the still water depth; U is the depth-averaged velocity vector; g is the acceleration due to gravity; $\mathbf{k}$ is the vertical unit vector; and $f = 2\Omega \sin \phi$ is the Coriolis parameter, in which Ω is the angular speed of the Earth and ϕ is the latitude. p_s is the atmospheric pressure at the free surface (interpolated from 0.50° hourly CFSv2 (Saha et al., 2014) mean sea level pressure fields) and ρ_0 is the reference density of water. The quantity ζ_{EQ} is the equilibrium tide, and ζ_{SAL} is the ocean self-attraction and loading term (interpolated from FES2014 solutions (ftp://ftp.legos.obs-mip.fr/pub/FES2012-project/data/LSA/FES2014/). ∇M is the horizontal momentum diffusion approximated through the Smagorinsky closure model (Smagorinsky, 1963), τ_s is the free surface stress due to winds (computed from 0.25° hourly CFSv2 10-m wind fields applying Garratt's drag law (Garratt, 1977) with the drag coefficient set to an upper limit of 0.0035), and τ_b is the stress at the seabed applying a spatially constant drag coefficient of 0.0025. $\sigma(x)$ are the spatially varying coefficients in the absorption-generation sponge layer region defined near the lateral open boundary (indicated in Figure 1). $\sigma(x)$ are a quadratic function of distance from the sponge layer edge, with the magnitude dependent on sponge layer width and depth, and a user-defined strength (Pringle, Wirasaet, Suhardjo, et al., 2018). ζ_c and U_c are the free surface and velocity tidal reference solutions that are applied in the sponge layer, which are reconstructed from TPXO9.1 harmonic tidal constituents (http://volkov.oce.orst.edu/tides/global.html).

The terms described above are all present in the typical 2DDI-BT (barotropic) mode. Including the following three terms, computed using information obtained from the GOFS 3.1 model, invokes the 2DDI-BC coupled mode:

1. ∇B is the depth-integrated baroclinic pressure gradient:

$$\nabla B = \int_{-h}^{\zeta} \left(g \nabla \left[\int_{z}^{\zeta} \frac{\rho - \rho_0}{\rho_0} dz \right] \right) dz, \tag{3}$$

where ρ is the density field, which is reconstructed from GOFS 3.1 salinity and temperature fields using the GSW Oceanographic Toolbox (McDougall & Barker, 2011). Note that the ζ upper limit on the integral is obtained from the ADCIRC model during the simulation at each time step. This is the main driver of ocean baroclinicity in the 2DDI-BC ADCIRC model.

2. ∇D is the depth-integrated momentum dispersion:

$$\nabla D = \nabla \int_{-h}^{0} [(\boldsymbol{v} - \boldsymbol{V}) \cdot (\boldsymbol{v} - \boldsymbol{V})] \, dz, \tag{4}$$

where v and V are the depth-resolving and depth-averaged GOFS 3.1 velocity fields, respectively. Although velocities between GOFS 3.1 and ADCIRC are not likely to be consistent, computing ∇D solely from the GOFS 3.1 velocities and passing them to ADCIRC acts like an additional dissipation term.

3. C is the dissipation tensor due to the energy conversion from barotropic tides to baroclinic internal tides using the local generation formulation (Pringle, Wirasaet, Suhardjo, et al., 2018; Pringle, Wirasaet, & Westerink, 2018):

$$C = C_{it} \frac{[(N_b^2 - \omega^2)(\tilde{\mathrm{N}}^2 - \omega^2)]^{1/2}}{4\pi\omega} (\nabla h \cdot \boldsymbol{U_T}) \nabla h, \tag{5}$$

where $U_{\boldsymbol{T}}$ is the depth-averaged tidal velocity vector, C_{it} is a scale factor set to 4.0, ω is set to the angular frequency of the M_2 tidal constituent, N_b (seabed) and $\tilde{\mathrm{N}}$ (depth-averaged) are the buoyancy frequencies computed from the GOFS 3.1 salinity and temperature fields using the GSW toolbox. $C = 0$ where $h < 100$ m to prevent excessive dissipation on the continental shelves (Pringle, Wirasaet, Suhardjo, et al., 2018). Furthermore, N_b is used to define the criticality of topography in order to limit energy conversion over supercritical topography (Pringle, Wirasaet, & Westerink 2018). Note that $U_{\boldsymbol{T}}$ is quite different from U even in deep water due to the presence of geostrophic ocean currents from the application of ∇B. Thus, $U_{\boldsymbol{T}}$ is determined from a 25-hr lagged moving average filter (Arbic et al., 2010; i.e., $\boldsymbol{U_T} = \boldsymbol{U} - \overline{\boldsymbol{U}}$, where $\overline{\boldsymbol{U}}$ is the filtered velocity). The value of C_{it} was selected from the results of 2DDI-BC simulations varying C_{it} (2.5, 4.0, 5.0). $C_{it} = 4.0$ gives the smallest mean *RMSE* tidal discrepancy from the tide gauge observations (see Table S1).

In this study, the terms and values coming from the GOFS 3.1 product (∇B, ∇D, N_b, $\tilde{\mathrm{N}}$) are first calculated on the GOFS 3.1 structured grid output which has 1/12° uniform horizontal resolution and is defined on 40 standard depth layers down to $h = 5{,}000$ m in the vertical direction. When horizontal gradients need to be computed (∇B and ∇D), second-order central finite-differencing is used. Depth-integration is achieved using the trapezoidal rule. The terms are then interpolated onto the unstructured ADCIRC mesh using bilinear spatial interpolation and are set to zero in regions where the GOFS 3.1 structured grid has no data nearshore. Furthermore, the terms are linearly interpolated in the temporal dimension at each computational time step.

It is noted here that the sponge layer region applied at the lateral open boundary (Figure 1) is critical to absorb outgoing oceanic information to avoid artificial reflections that contaminate the solution. Forcing terms not associated with tidal solutions (∇B, ∇D, τ_s, p_s) are set to zero (p_s is set to the background value, 1,013 hPa) within the sponge layer. Additionally, the GOFS 3.1 free surface output is added onto the tidal elevation solutions in ζ_c. This aids in accounting for nonlocal variations controlled by global ocean dynamics. No component from GOFS 3.1 is added to U_c.

2.3. Simulation Setup and Computational Times

The 2DDI ADCIRC model simulations were conducted over a 13-month time period beginning on 1 December 2016 and ending on 1 January 2018. The first month was used for spinning-up the astronomical, atmospheric, and baroclinic forcings. The model time step was set to 1.2 s to ensure that the Courant-Friedrichs-Lewy constraint was met.

Simulations were conducted using 960 computational cores (1,500–1,700 mesh vertices per core, which is at the edge of the scalability limit for ADCIRC under the explicit lumped mass matrix scheme, Tanaka

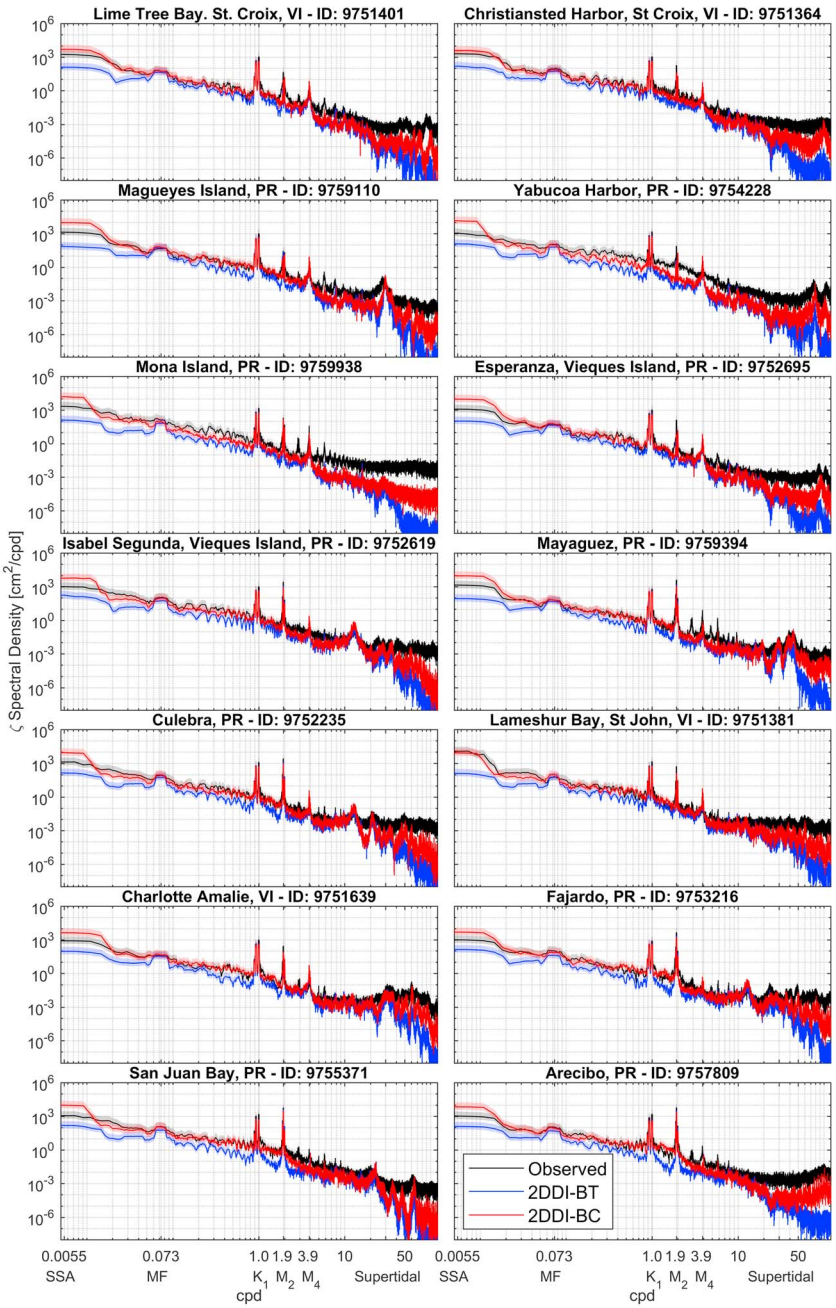

Figure 3. Power spectral densities of 6-min sea level variations at the National Oceanic and Atmospheric Administration/National Ocean Service tide gauges in the Puerto Rico and the U.S. Virgin Islands region for the year of 2017 comparing observations with the 2DDI-BT and 2DDI-BC model simulations. The lines indicate the mean, and the translucent bands indicate the 95% confidence intervals in the spectral density estimate. 2DDI-BT = two-dimensional depth-integrated barotropic mode; 2DDI-BC = baroclinic-coupled 2DDI; SSA = semiannual; MF = fortnightly; cpd = cycles per day.

et al., 2011, employed here) of a high-performance computing machine with Haswell processors and a Mellanox FDR Infiniband network connection. To complete the 13 months of simulation time, 2DDI-BT takes ≈33 wall-clock hours and 2DDI-BC takes ≈37 wall-clock hours. Thus, the baroclinic coupling accounts for roughly 12% additional wall-clock time related to; reading the primitive variables (temperature, salinity, and velocity) from the GOFS 3.1 3-hourly NetCDF output file, converting the primitive variables into the necessary terms for coupling (∇B, ∇D, N_b, $\tilde{N}$), and interpolation of the terms to the unstructured mesh in time and space.

2.4. Observational Data

All 14 NOAA/National Ocean Service tide gauges located around the PRVI region that were in operation during 2017 (Figure 2) are used to assess the model performance. Six of the tide gauges (IDs: 9751381, 9752235, 9754228, 9755371, 9757809, 9759938) have water elevation records spanning all 12 months of 2017. Hence, these tide gauges are selected for plots of yearly elevation time series in section 3.1.3. Note that Arecibo (ID: 9757809) has a month long gap in the signal from the latter part of September due to Hurricane Maria. The other eight tide gauges have no water elevation records from the latter part of September or the beginning of October for the rest of 2017. Table S1 contains the tide gauge locations which have been slightly adjusted from the listed locations to ensure that they are completely submerged in the model.

3. Results

3.1. Analysis of Coastal Sea Level Variations

This section analyzes the entire frequency spectrum of (nonwind wave) 6-min coastal sea level variations around PRVI. First, spectral density plots are initially shown and briefly described. This is followed by a more detailed analysis of model performance across the individual frequency bands.

3.1.1. Spectral Densities

The frequency content of the coastal sea level variations at the tide gauges in the PRVI region for 2017 is introduced through spectral density plots (Figure 3). The *pmtm* MATLAB function which implements Thomson's multitaper power spectral density method (Thomson, 1982) is used with default settings. The slope of the spectral density spectrum is well represented by both versions of the 2DDI model. Peaks at pertinent tidal frequencies (fortnightly [MF], diurnal [K_1], semidiurnal [M_2], and semi-semidiurnal [M_4], etc.) are clearly reproduced. Averaged across the tide gauges, the spectral energy integrated over the frequency range between 1/183 and 120 cycles per day is increased from 54 to 96 cm^2 when ocean baroclinicity is incorporated in the 2DDI model, nudging the modeled spectral densities closer toward those of the observations (120 cm^2, see Table S1 for integrated spectral energy values). In the subtidal and intratidal range (between the K_1 and M_4 peaks), the 2DDI-BC model simulation is in good agreement at most tide gauges, however the modeled spectral density within the intratidal range at Yabucoa Harbor (ID: 9754228), and within the MF to K_1 frequency range at Mona Island (ID: 9759938), remains visually smaller than observations.

At most locations the spectral density at the semiannual (SSA) frequency for the 2DDI-BC model simulation appears overestimated, however the length of simulation is probably too short to obtain an accurate estimate here particularly because observations feature gaps in the data while the simulations do not. In fact, analyses in section 3.1.3 indicate that the intra-annual (seasonal) variation is generally well represented.

At the supertidal frequencies both 2DDI model implementations appear deficient at most tide gauges, although the spectrum is relatively flat in the observations which may be indicative of instrument noise (Savage et al., 2017). Indeed, the model appears to roughly mimic the frequencies at which peaks in the observed signal are apparent. Associated supertidal shelf-resonant seiching is analyzed in section 3.1.5.

3.1.2. Tidal Elevations

Tidal elevations shown in this section and in section 3.1.3 were computed using a least-squares tidal harmonic analysis for the model simulations (using the ADCIRC built-in solver) and observations (using UTide; Codiga, 2011) requesting the following 12 constituents: SA, SSA, MM, MF, Q_1, O_1, P_1, K_1, N_2, M_2, S_2, K_1.

The amplitude and phase diagrams of the modeled (both 2DDI-BT and 2DDI-BC) major semidiurnal (M_2) and diurnal (K_1) tidal constituents around PRVI are illustrated in Figure 4. The TPXO9.1 tidal solutions as well as observed tidal amplitudes at the tide gauges are also shown for reference. There is an amphidrome in the M_2 tide located southeast of mainland Puerto Rico resulting in small M_2 tidal amplitudes in the southern PRVI region. Along the northern coasts of Puerto Rico the M_2 tidal amplitude ranges between 10 and 18 cm. In comparison the K_1 tides vary little across the PRVI region ranging between 6 and 10 cm throughout.

One of the major differences between 2DDI-BT and 2DDI-BC is the position of the M_2 amphidrome, which is originally situated near the southeast corner of Puerto Rico in the 2DDI-BT simulation. In 2DDI-BC this amphidrome has moved further offshore in the southwest direction. The amphidromic position according to the TPXO9.1 solutions is even further offshore, but in the southeast direction, at approximately 16.4°N 64°W (bottom right hand corner of Figure 4). Comparing 2DDI-BC to 2DDI-BT, the M_2 phase lag is shifted by 10–17° in the majority of locations across PRVI region, and by as large as 120° in Yabucoa Harbor (ID: 9754228) which is close to the amphidrome. Further, the M_2 tidal amplitudes on the northern coast are

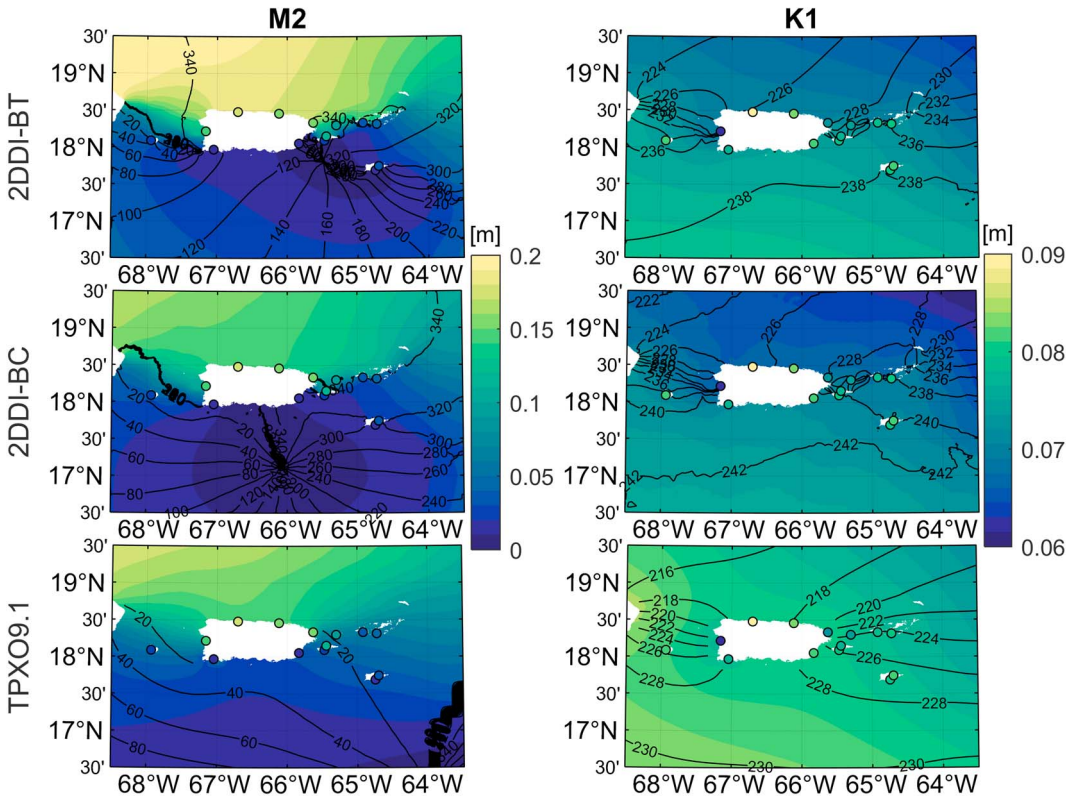

Figure 4. Modeled (top row is 2DDI-BT; second row is 2DDI-BC which includes a parameterization of internal tide energy conversion) amplitude (colors) and phases (contour lines) of the dominant semidiurnal (M_2) and diurnal (K_1) tidal constituents around PRVI for 2017. The colored circles indicated the observed tidal amplitudes at the National Oceanic and Atmospheric Administration/National Ocean Service tide gauges. Bottom row are the interpolated TPXO9.1 tidal solutions. 2DDI-BT = two-dimensional depth-integrated barotropic mode; 2DDI-BC = baroclinic-coupled 2DDI.

decreased by 3–4 cm. The effect on the K_1 tides is comparatively small—the mean amplitudes in the PRVI region decreased by just 0.32 cm. The main take away point here is the sensitivity of the M_2 tide around PRVI due to the inclusion of ocean baroclinicity with internal tide conversion parameterization is significant, especially with regards to the phasing.

It is found that the inclusion of ocean baroclinicity with internal tide conversion parameterization generally decreases the M_2 tidal amplitudes. While this appears to be in closer agreement to the TPXO9.1 solutions (Figure 4), the mean M_2 absolute amplitude error against tide gauge observations is slightly smaller in 2DDI-BT (1.2 cm) compared to 2DDI-BC (1.6 cm) (Table S1). However, the M_2 phase lag is shifted closer toward the observed values at all but one tide gauge for 2DDI-BC (averaged absolute M_2 phase lag error is 27° compared to 41° for 2DDI-BT, Table S1). This ultimately results in a smaller overall tidal discrepancy versus observations (quantified in section 3.2). The C_{it} scale factor used here was tuned to try and minimize this overall discrepancy, but we believe that there are still improvements that can be made to better account for the varying dissipative effects (both internal tide energy conversion and bottom friction) to further reduce the tidal discrepancy in this new computational domain.

3.1.3. Seasonal Coastal Sea Level Variations

The spectral density of low frequency subtidal coastal sea level variations when the baroclinic coupling was included are shown to be largely in good agreement with observations (Figure 3). Here, we present an analysis of the intra-annual or seasonal cycle, driven by large-scale ocean dynamics, observed during 2017.

A significant proportion of the subtidal variability can be classified as seasonal in the Caribbean region; Torres and Tsimplis (2012) approximated the variance explained by the seasonal harmonics to be between 35% and 55% around PRVI. To initially demonstrate the seasonal effect, modeled and observed (at tide gauges) annual (SA) and SSA harmonic constituents around PRVI for 2017 are illustrated (Figure 5). The ampli-

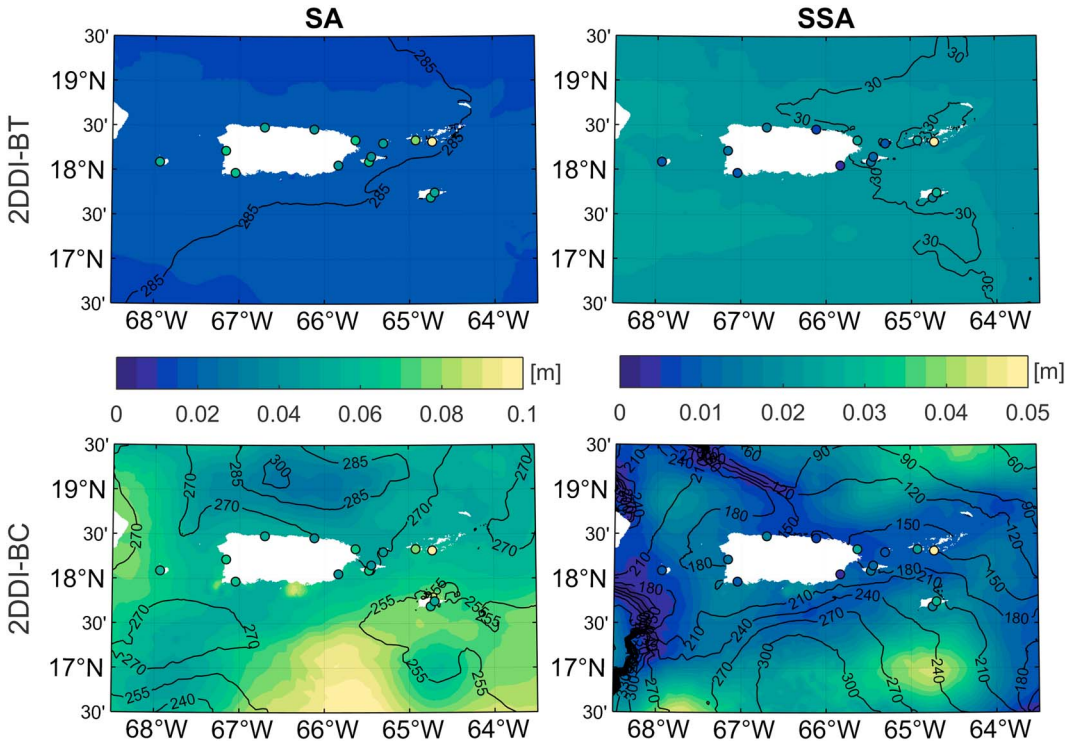

Figure 5. Modeled (top palettes are 2DDI-BT; bottom palettes are 2DDI-BC) amplitude (colors) and phases (contour lines) of the SA and SSA harmonic constituents around PRVI for 2017. Note that the phase of SA is referenced to the calendar year. The colored circles indicated the observed tidal amplitudes at the National Oceanic and Atmospheric Administration/National Ocean Service tide gauges. 2DDI-BT = two-dimensional depth-integrated barotropic mode; 2DDI-BC = baroclinic-coupled 2DDI; SA = annual; SSA = semiannual.

tude and phase of the seasonal constituents from the 2DDI-BT simulation varies little across PRVI and is induced primarily as a result of seasonal atmospheric pressure oscillations. The phase of the SA constituent illustrated here is referenced to the calendar year, indicating that the peak occurs around mid-September. Without ocean baroclinicity the mean amplitude of both constituents throughout PRVI is roughly 2 cm. In comparison, the 2DDI-BC simulation induces a far more varied seasonal signal across PRVI. Including ocean baroclinicity increases the mean amplitudes of the SA constituent to 5.9 cm and, interestingly, decreases the mean amplitude of the SSA constituent to 1.1 cm, which is in closer agreement to the observations. Comparing 2DDI-BT to 2DDI-BC, the mean absolute error of the SA amplitudes is reduced from 4.7 to 1.7 cm, while for the SSA amplitude it is reduced from 1.1 to 0.96 cm (Table S1). Similarly, the mean absolute phase lag error for SA is reduced from 27° to 14°, although for SSA it is increased from 64° to 91° (Table S1). However, SSA phases of the observations are highly varied between the tide gauges (range from 40° to 321°) in comparison to the phases of the modeled results (range from 29° to 33° [2DDI-BT] and 152° to 228° [2DDI-BC]), so their reliability is unclear. This is likely related to the length of the observed time series, some of which does not even span the full calendar year.

The modeled and observed seasonal cycle at the tide gauges (those with observations spanning the full calendar year) are shown with more granularity than the seasonal constituent diagrams using a 30-day moving mean time series (Figure 6). The GOFS 3.1 model results are also included for comparison (these were obtained from the nearest wet grid point to a tide gauge). As inferred from the seasonal constituents the 2DDI-BT simulation does induce a peak in the sea level around middle to late September, in addition to a low at the beginning of July and a local high at the beginning of April. When ocean baroclinicity is incorporated the peak in sea level becomes more pronounced and occurs earlier in September at the Puerto Rico tide gauges. Interestingly, this is a followed by a local low in the sea level early October before another local peak in the sea level around mid-November. It will be shown later (section 3.1.4) that this sea level setdown around early October can be attributed to the lasting effects of Hurricane Maria (made landfall in Puerto Rico on 20 September) on the vertical density structure of the water column. The lowest sea levels occur

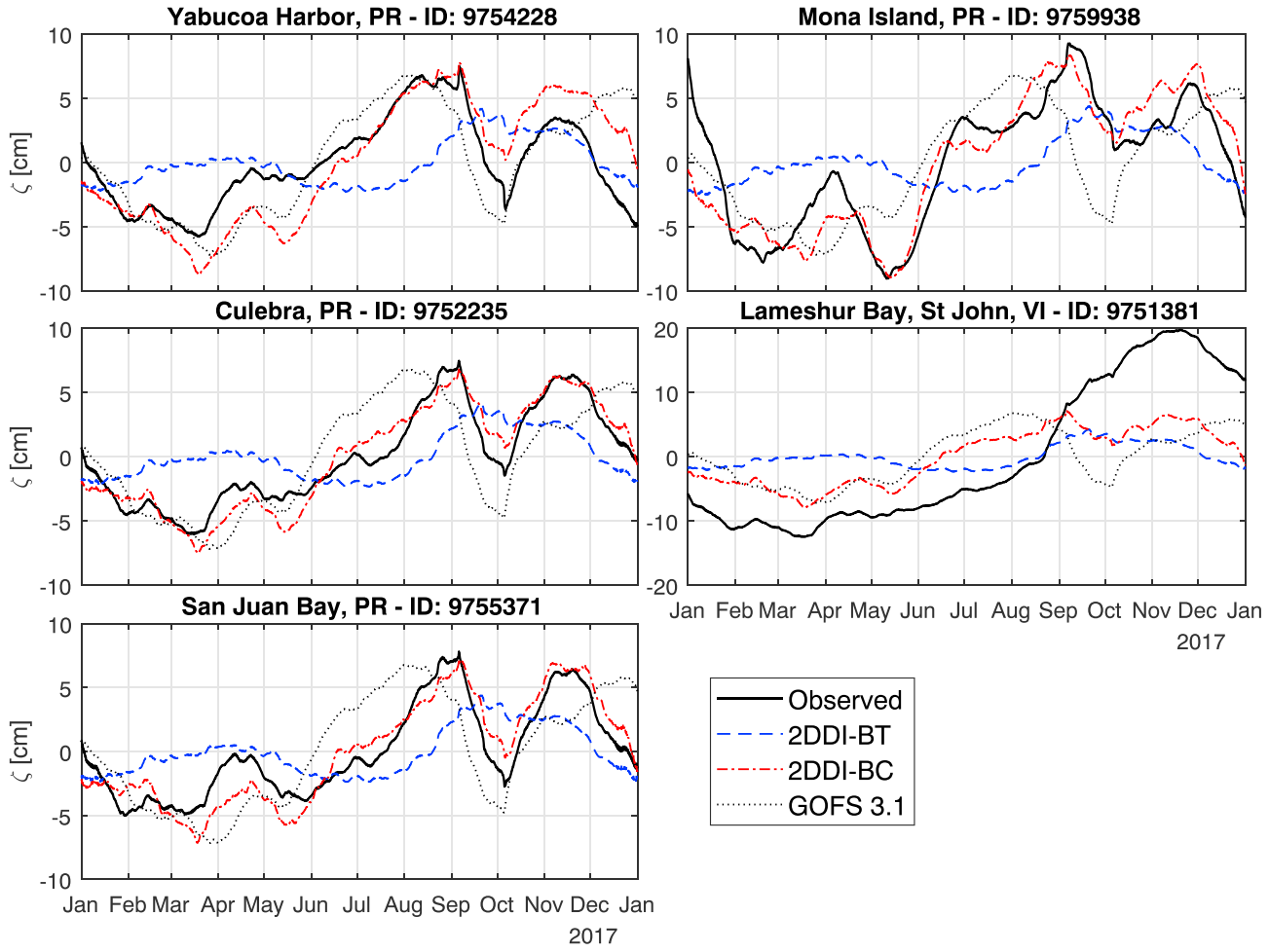

Figure 6. 30-day moving mean sea level variations at the NOAA/NOS tide gauges (that have complete signals throughout 2017) in the PRVI region comparing observations with the 2DDI-BT and 2DDI-BC ADCIRC model simulations, and the GOFS 3.1 model outputs. Note that these are demeaned sea levels where the mean has been calculated independently for each time series over the year. 2DDI-BT = two-dimensional depth-integrated barotropic mode; 2DDI-BC = baroclinic-coupled 2DDI; GOFS = Global Ocean Forecast System.

around mid-March at all tide gauges, and Mona Island (ID: 9759938) also has low sea levels around mid-May. At Lameshur Bay (ID: 9751381), the highest sea levels occur around mid-November but this is not well represented by any of the model simulations (including GOFS 3.1). Aside from Lameshur Bay, 30-day moving mean yearly time series from the 2DDI-BC simulation are in good agreement with the observations. Omitting Lameshur Bay, the mean *RMSE* in the 30-day moving mean yearly time series is 1.9 cm (SD = 0.62 cm) for 2DDI-BC, compared to 3.5 cm (SD = 0.63 cm) for 2DDI-BT and 3.3 cm (SD = 0.49 cm) for GOFS 3.1 (Table S1). Thus, the agreement of 2DDI-BC with observations is superior to that of the GOFS 3.1 ocean model used to force the baroclinicity and lateral open boundary conditions in the sea level. This is an important result because it indicates that the 2DDI-BC model could be used to downscale global ocean sea levels for improved accuracy at the coast where fine scales are vital.

3.1.4. Local Subtidal Coastal Sea Level Variations and Surge

The spectral density of high-frequency subtidal and intratidal coastal sea level variations when the baroclinic coupling was included are shown to be in largely good agreement with observations (Figure 3). Here, we present an analysis of the local primary surge and subtidal response.

Of particular interest for the PRVI region is the nontidal response in the coastal sea level during September 2017 when Category 5 Hurricanes Irma and Maria struck in quick succession (Figure 7). The nontidal residual for the observations and the 2DDI model simulations were obtained by subtracting the reconstructed tidal harmonics. The tidal harmonic analysis and reconstruction was conducted with UTide employing the "auto" option, which automatically selects 59 tidal constituents that best account for the tidal variance.

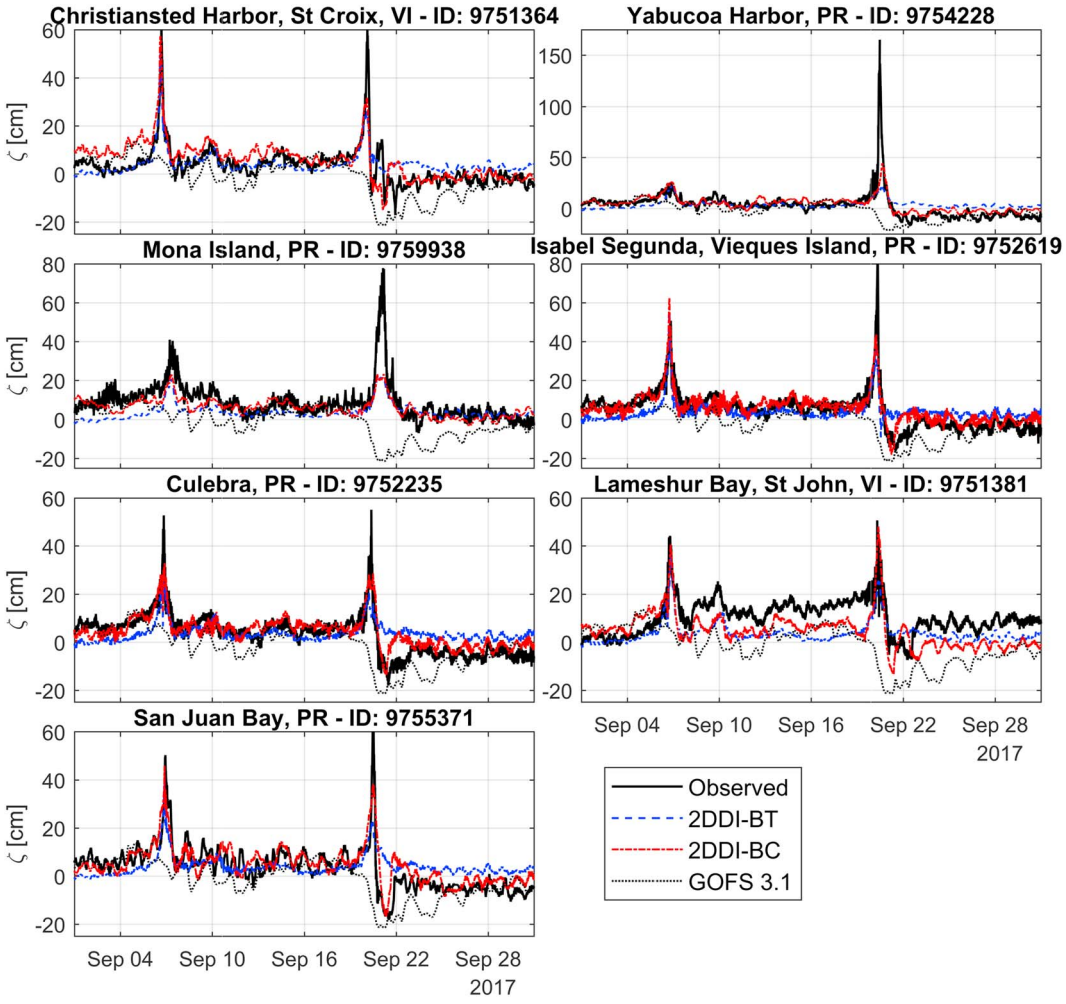

Figure 7. Nontidal residual in the sea level during September 2017 at the National Oceanic and Atmospheric Administration/National Ocean Service tide gauges (that have complete signals throughout September 2017) in the PRVI region comparing observations with the 2DDI-BT and 2DDI-BC ADvanced CIRCulation model simulations, and the GOFS 3.1 model outputs. Note that these are demeaned sea levels where the mean has been calculated independently for each time series over the year. 2DDI-BT = two-dimensional depth-integrated barotropic mode; 2DDI-BC = baroclinic-coupled 2DDI; GOFS = Global Ocean Forecast System.

The signal-to-noise ratio threshold was set to 2 (default) which did not result in reducing the number of tidal constituents below 59 for any tide gauge. No linear trend was used and the amplitude of the seasonal constituents were set to zero before reconstruction. The GOFS 3.1 model output does not include tides.

As expected the 2DDI model (both BT and BC versions) is well adept at capturing the primary surge processes, while the GOFS 3.1 model does not capture the surge. It is worth mentioning that the primary surge is very sensitive to the atmospheric forcing. Here, CFSv2 forcing is used which underestimates the minimum central pressure and overestimates the size of both storms (Joyce et al., 2019). Thus, for example, the peak surge at Yabucoa Harbor (ID: 9754228), which was in the direct path of Hurricane Maria and predominantly sensitive to the pressure deficit (Joyce et al., 2019), cannot be captured sufficiently. The effects of setup due to wind waves is also important in certain areas (Joyce et al., 2019). At some of the tide gauges (IDs: 9751364, 9752619, 9752235, 9755371), the peak surge during Hurricane Irma is larger in the 2DDI-BC simulation than the 2DDI-BT simulation predominantly because of an 8–10 cm pre-storm offset in background sea levels. More interestingly, the peak surge height at most of the tide gauges (except for Mona Island, ID: 9759938) during Hurricane Maria is larger in the 2DDI-BC simulation by 10–20 cm despite similar pre-storm sea levels.

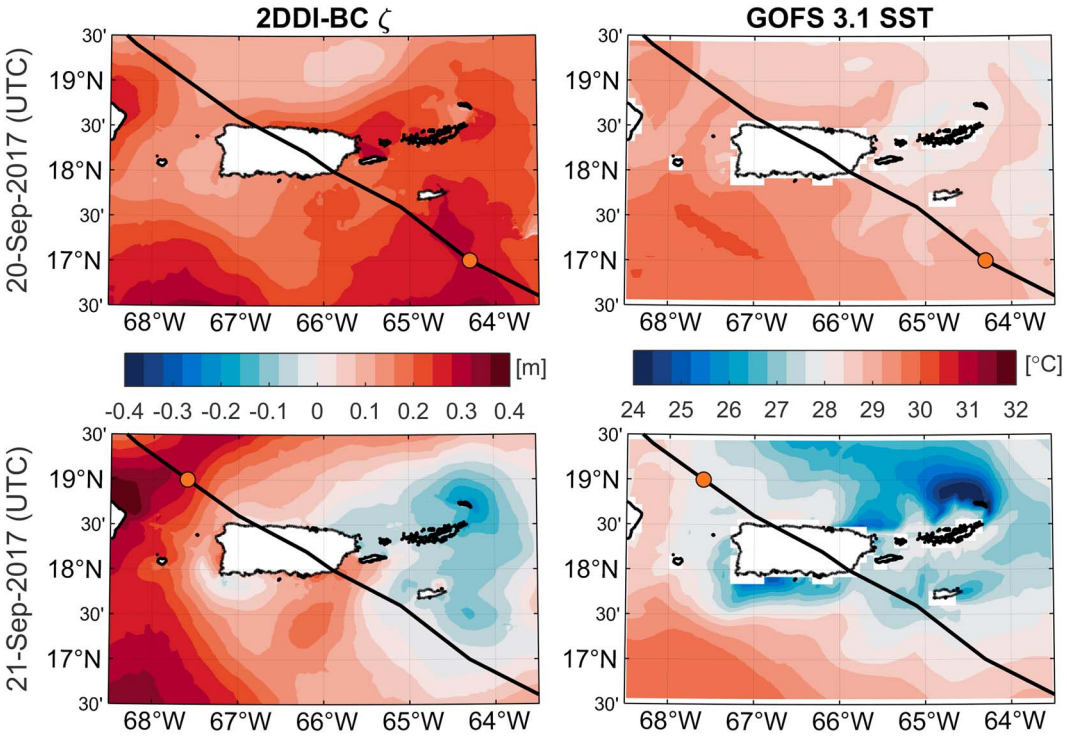

Figure 8. (left) Demeaned (mean is calculated over the calendar year) nontidal sea level in the Puerto Rico and the U.S. Virgin Islands region as simulated by the 2DDI-BC model upon approach of Hurricane Maria (top), and on retreat (bottom). (right) SST as simulated by the GOFS 3.1 model at the same times as the left palettes. The thick black line indicates the best track of Hurricane Maria and the orange circle indicates its location at the corresponding time. 2DDI-BC = two-dimensional depth-integrated baroclinic mode; GOFS = Global Ocean Forecast System; SST = sea surface temperature.

Following Hurricane Maria there is a noticeable setdown in the coastal levels at all the tide gauges in Figure 7 except for Mona Island (ID: 9559938). At some of the tide gauges (IDs: 9752619, 9755371, 9752235, 9751381) the sea levels drop quite dramatically just after the storm on 21 September before flattening off at approximately 10 cm below the pre-storm level (pre-storm level ≈ +5 cm, post-storm ≈ −5 cm). This setdown effect is captured by the 2DDI-BC and GOFS 3.1 models but it is not captured by the 2DDI-BT model simulation. Thus, it can be presumed that the setdown is induced by the local baroclinicity. To demonstrate this, the nontidal sea levels throughout the region during the 2DDI-BC simulation and the sea surface temperature (SST) simulated by the GOFS 3.1 model on 20 September 00:00 UTC as the storm approaches PRVI, and on September 21 00:00 UTC after the storm has passed over Puerto Rico, are shown in Figure 8. As the storm approaches the SST is approximately 28–29 °C over PRVI and the sea level is 0.1–0.3 m above the yearly mean. Note that a higher sea level around the storm center is caused by the low atmospheric pressure. When the storm passes over the PRVI region it induces mixing of the warm surface waters with colder waters below the thermocline leaving a cold wake of SST (as illustrated in Figure 8 on 21 September 00:00 UTC) that can remain for weeks (Emanuel, 2001). Caribbean Coastal Ocean Observing System oceanographic buoy observations corroborate this effect where in San Juan a 5 °C drop in SST and increase in the surface salinity from 35.5 to 37.3 psu was measured following Hurricane Maria (Chardon-Maldonado et al., 2018), indicative of deep water upwelling to the top layers. These heavier surface waters induce a baroclinic pressure gradient pushing water away from those regions, causing a setdown which is most prominent northeast of the British Virgin Islands on 21 September 00:00 UTC. With regards to our region of interest, the setdown is most evident on the northeast of Puerto Rico and around the U.S. Virgin Islands (e.g., IDs: 9751364, 9752619, 9755371, 9752235, 9751381—Figure 7) and is also apparent in a small region on the southwest corner of Puerto Rico around Magueyes Island. A further encouraging observation is that a noticeable setdown was neither observed nor simulated by the 2DDI-BC model at Mona Island (ID: 9559938). On the other hand, the GOFS 3.1 model erroneously indicates a setdown perhaps due to insufficient resolution to distinguish between the offshore island and coastal Puerto Rico.

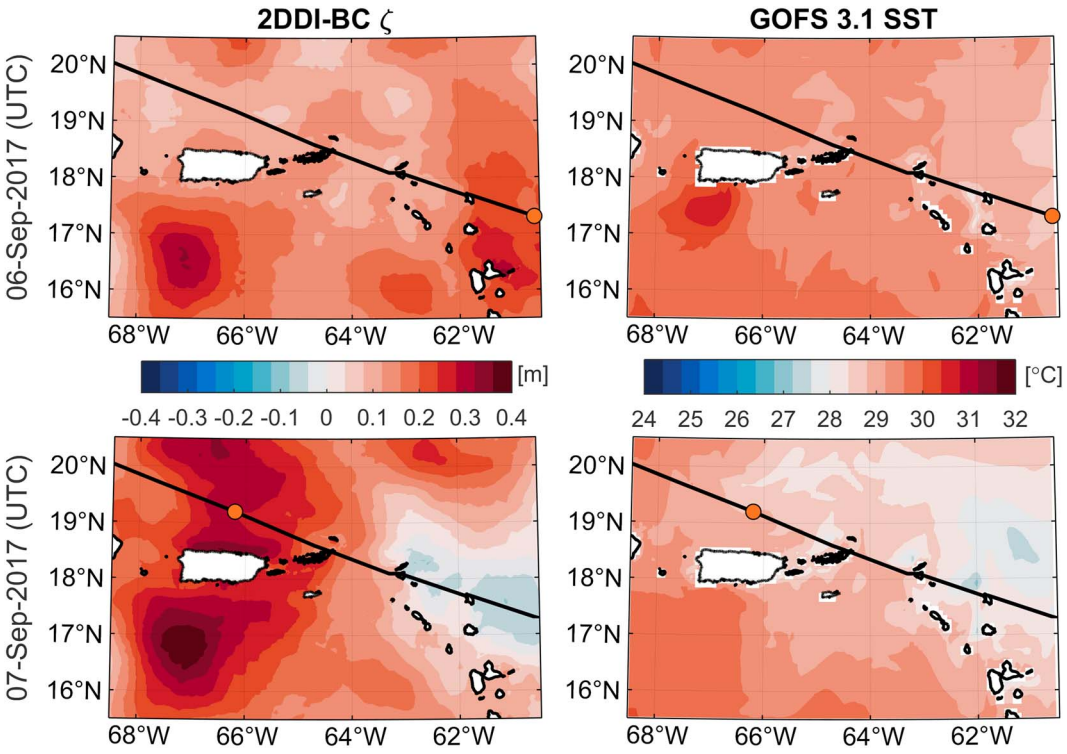

Figure 9. (left) Demeaned (mean is calculated over the calendar year) nontidal sea level in the Puerto Rico and the U.S. Virgin Islands and northern Lesser Antilles region as simulated by the 2DDI-BC model upon approach of Hurricane Irma (top), and on retreat (bottom). (right) SST as simulated by the GOFS 3.1 model at the same times as the left palettes. The thick black line indicates the best track of Hurricane Irma and the orange circle indicates its location at the corresponding time. 2DDI-BC = two-dimensional depth-integrated baroclinic mode; GOFS = Global Ocean Forecast System; SST = sea surface temperature.

It is apparent in the time series of the nontidal residuals (Figure 7) that a measurable setdown adjacent to PRVI was not observed in the aftermath of Hurricane Irma. This is explained by the difference in the hurricane tracks. Compared to Maria, Irma tracks relatively far north of the PRVI region (Figure 9) away from its shallow areas. The SST was reduced from around 30 °C before the storm to 28–29 °C after the storm (this SST state appears to remain until Hurricane Maria strikes the region). While negligible setdown occurred in the PRVI region due to baroclinicity during Hurricane Irma, according to our model simulations there is an observable cooling of the ocean surface and setdown on the northern islands of the Lesser Antilles chain east of PRVI (Figure 9) that Hurricane Irma directly passes over.

3.1.5. Supertidal Coastal Sea Level Variations

The supertidal sea level spectrum at frequencies between 0.5 and 5 cycles per hour are shown in Figure 10. Here, the *pmtm* MATLAB function is used with 4,097 frequency columns. As described earlier the background energy is larger in the observations than the 2DDI model. However, certain peaks in the observed spectral densities clearly standout in the observations at a number of tide gauges. Based on coarse estimates of the shelf geometry (length, L, and mean depth, h; these are included in Table S1 for each tide gauge), it would appear that the periods at which the main peaks are observed occur at the fundamental resonant period, T_R of the shelf (indicated in Figure 10 by the vertical dashed lines):

$$T_R = \frac{4L}{\sqrt{gh}}. \tag{6}$$

The shelf is very narrow on St. Croix and Mona Island so T_R is estimated from equation (6) to be less than 12 min at the tide gauges located here, which is above the Nyquist frequency limit for 6-min observations. Indeed, no excitation is observed nor modeled at Lime Tree Bay (ID: 9751401), Christiansted Harbor (ID: 9751364), or Mona Island (ID: 9759938). Although the shelf around Lameshur Bay (ID: 9751381) is not particularly narrow, no observable shelf-resonance was found to develop there. Using the distance from

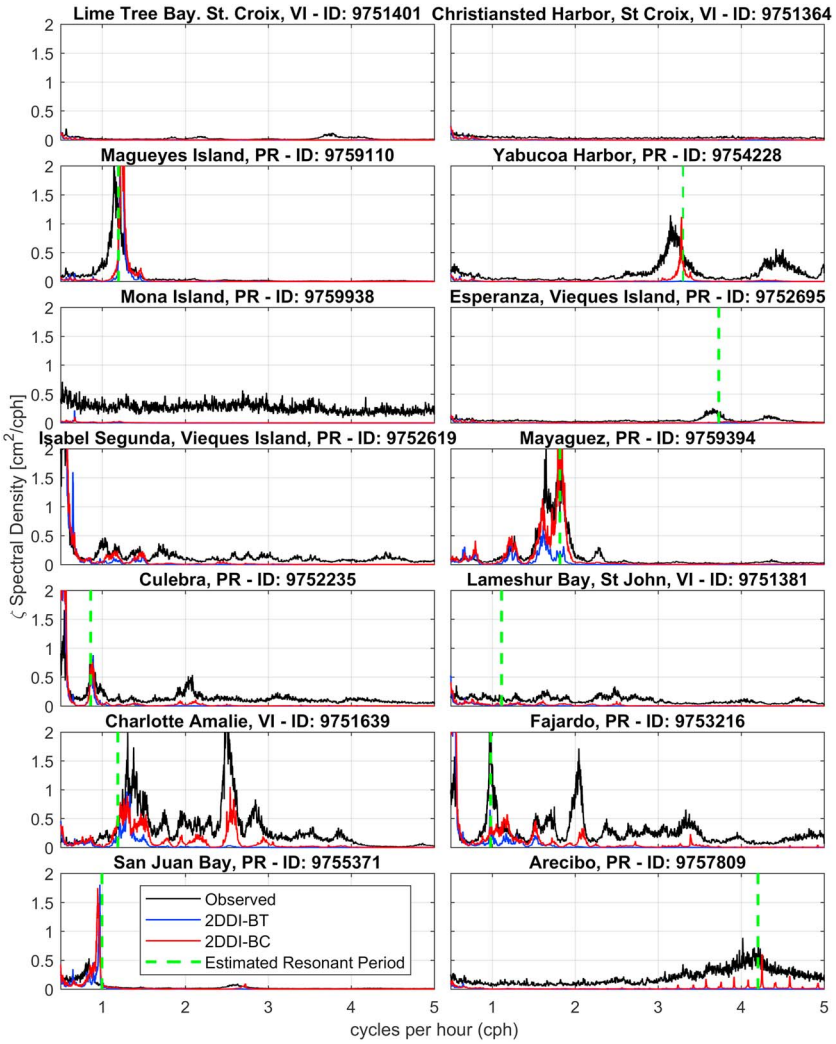

Figure 10. Supertidal power spectral densities of the 6-min sea level variation at the National Oceanic and Atmospheric Administration/National Ocean Service tide gauges in the PRVI region for the year of 2017 comparing observations with the 2DDI-BT and 2DDI-BC model simulations. Vertical dashed lines indicate an estimate of the period of the fundamental normal shelf mode (T_R) using equation (6). 2DDI-BT = two-dimensional depth-integrated barotropic mode; 2DDI-BC = baroclinic-coupled 2DDI.

Culebra (ID: 9752235) to Vieques Island instead of the distance to the shelf break can better estimate T_R through equation (6) that was observed and modeled here (≈70 min). At Fajardo (ID: 9753216), two resonant peaks appear. One peak is at $T_R \approx 60$ min as indicated by the dashed line in Figure 10, which was estimated using the shelf distance to the Fajardo port area. The other peak at $T_R \approx 30$ min can be estimated using the shelf distance to the ocean-facing peninsula north of Fajardo, on the northeasternmost corner of the Puerto Rico mainland. While no resonance is found in the observations at San Juan Bay (ID: 9755371), model simulations show some excitation near the estimated T_R. There may be additional damping due to port structures, lagoons, bottom friction, and channels connected to the bay that are not fully accounted for by the model.

Shelf-resonant seiching along the Carribbean coast of Puerto Rico has been previously described (Giese et al., 1990), in which $T_R = 50$-min oscillations at Magueyes Island (ID: 9759110) were thoroughly explored. It was argued that such seiches are excited by internal waves generated by strong tides in the southeastern Caribbean (Giese et al., 1990). However, it is not possible for either versions of the 2DDI model to induce supertidal excitation due to internal tides directly. Further, GOFS 3.1 does not simulate tides ruling out indirect effects in 2DDI-BC. Certainly, the only mechanism for 2DDI-BT to reproduce seiching is through the meteorological forcing—model simulations conducted with or without tidal forcing were found to give

essentially identical supertidal spectral densities ruling out the direct influence of barotropic tides on seiching. Note that it is not our intent to comment on the validity of attribution to shelf-resonant seiching in the region but merely to point out that excitation of the modes must be primarily induced in the 2DDI models due to the hourly meteorological forcing.

3.2. Model Skill Evaluation

In this section the model skill for both 2DDI model implementations is evaluated, first, over the entire year considering both the full and nontidal residual time series (section 3.2.1). Second, the performance and model skill for the model (with the inclusion of tides) during the month of September when the twin hurricanes struck is evaluated (section 3.2.2). Comparison to a zero mean offset between the 2DDI-BT model simulation and observations is conducted.

The following metrics are used to evaluate the performance of a model run at a particular tide gauge:

$$\gamma^2 = \frac{var(\zeta_m - \zeta_o)}{var(\zeta_o)}, \tag{7}$$

$$Skill = 1 - \frac{\int_0^T (\zeta_m - \zeta_o)^2 dt}{\int_0^T \left(|\zeta_m - \overline{\zeta_o}| + |\zeta_o - \overline{\zeta_o}|\right)^2 dt}, \tag{8}$$

$$RMSE = \left[\frac{1}{T}\int_0^T (\zeta_m - \zeta_o)^2 dt\right]^{1/2}, \tag{9}$$

in which T is the time period of assessment, the subscripts "o" and "m" represent observed and modeled values, respectively, the overline represents the temporal mean, and *var* represents the temporal variance. γ^2 (Kodaira et al., 2016) is the normalized variance of the error, where a value of 0 represents perfect agreement and a value of 1 represents no better than constant (γ^2 can exceed 1), and *Skill* (Willmott, 1981) is an "index of agreement" measuring model skill (a value of 1 represents perfect agreement and a value of 0 represents complete disagreement). *RMSE* is the root-mean squared-error, which is composed of (linear) systematic ($RMSE_s$) and (random) unsystematic ($RMSE_u$) components (Willmott, 1981):

$$RMSE_s = \left[\frac{1}{T}\int_0^T (\hat{\zeta_m} - \zeta_o)^2 dt\right]^{1/2} \qquad RMSE_u = \left[\frac{1}{T}\int_0^T (\zeta_m - \hat{\zeta_m})^2 dt\right]^{1/2}, \tag{10}$$

where $\hat{\zeta_m}$ is the linear regressed prediction for each observation, i.e., $\hat{\zeta_m} = a + b\zeta_o$, in which a and b coefficients are found through standard least squares regression.

3.2.1. Model Error Metrics for 2017

The error metrics of the yearlong 2DDI-BT and 2DDI-BC model simulations for the full signal including tides and for the nontidal residual at the PRVI tide gauges are shown in Figure 11. All error metrics here are calculated based on demeaned sea levels where the mean is calculated independently for each time series over the year (the standard deviation in the yearly mean sea level is ≈3 cm across all the tide gauges). The inclusion of ocean baroclinicity in the 2DDI-BC model simulation results in smaller errors (higher *Skill*) at all 14 tide gauges compared to the 2DDI-BT model simulation. In summary, for the full signal averaged across all tide gauges the mean *RMSE* is reduced from 7.3 cm (SD = 1.8 cm) to 5.6 cm (SD = 1.4 cm), the mean value of γ^2 is reduced from 0.42 (SD = 0.098) to 0.25 (SD = 0.078), and the mean *Skill* is increased from 0.87 (SD = 0.050) to 0.93 (SD = 0.033).

The differences in γ^2 and *Skill* between the 2DDI-BT and 2DDI-BC model simulations are more apparent in the nontidal residual. Averaged across all tide gauges the mean value of γ^2 is reduced from 0.84 (SD = 0.096) to 0.51 (SD = 0.090), and the mean *Skill* is increased from 0.54 (SD = 0.084) to 0.85 (SD = 0.048). Thus, the inclusion of ocean baroclinicity allows the simulation to track the observations better over the course of the year as detailed in section 3.1.3. Although not directly comparable, to put the values of γ^2 computed on the nontidal residual in perspective, a previous study obtained $\gamma^2 \approx 0.75 - 0.85$ in the PRVI region (Kodaira et al., 2016). This study conducted 1/12° resolution baroclinic global ocean model simulations between 15 August and 30 October 2014.

Including ocean baroclinicity does not change the *RMSE* of the nontidal residual as significantly as it affects γ^2 and *Skill*—the mean *RMSE* is reduced from 5.4 cm (SD = 1.5 cm) to 4.3 cm (SD = 1.3 cm). We find

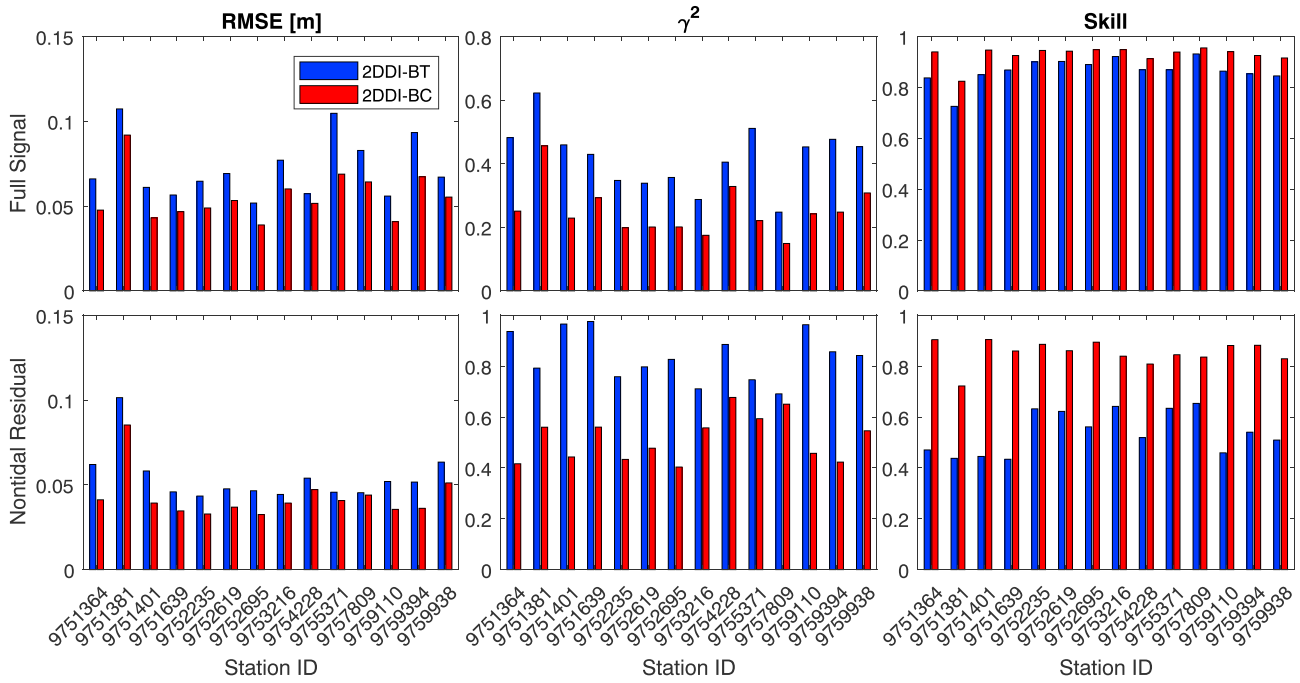

Figure 11. 2017 yearlong error metrics – RMSE (left), γ^2 (middle), *Skill* (right) – for the 2DDI-BT and 2DDI-BC model simulations versus observations at the 14 NOAA/NOS tide gauges in the PRVI region. Top: The full signal including tides, Bottom: The nontidal residual. 2DDI-BT = two-dimensional depth-integrated barotropic mode; 2DDI-BC = baroclinic-coupled 2DDI.

that is because the addition of ocean baroclinicity primarily aids in improving the *systematic* error in the 2DDI model: the mean $RMSE_s$ for the nontidal residual is reduced from 4.9 cm (SD = 1.6 cm) to 1.7 cm (SD = 1.8 cm). Thus, the total *RMSE* for the 2DDI-BC model is largely composed of unsystematic errors (mean $RMSE_u$ is 3.7 cm (SD = 0.45 cm) compared with 2.3 cm (SD = 0.20 cm) for 2DDI-BT) which are of less concern with regards to model fidelity. γ^2 and the *Skill* metric (Willmott, 1981) are somewhat capable of capturing this effect. For reference, note that when tides are included the mean $RMSE_s$ is 3.5 cm (SD = 1.6 cm) and 2.0 cm (SD = 1.7 cm) for the 2DDI-BT and 2DDI-BC models, respectively. The mean $RMSE_u$ is 6.2 cm (SD = 1.6 cm) and 5.0 cm (SD = 0.78 cm), respectively.

The mean tidal *RMSE* discrepancy computed from the eight major tidal constituents (Q_1, O_1, P_1, K_1, N_2, M_2, S_2, K_1) is reduced from 4.1 cm (SD = 2.5 cm) to 3.2 cm (SD = 1.3 cm) when ocean baroclinicity is included (Table S1). The effect of tides on the total *RMSE* (Figure 11) is most apparent at the tide gauges situated on the northern side of PRVI where the M_2 tidal amplitude is largest (Figure 4). The *RMSE* between the full signal and the nontidal residual is almost identical for tide gauges near the M_2 tidal amphidrome such as those located on St. Croix (IDs: 9751364, 971401).

3.2.2. Model Performance During Hurricanes Irma and Maria

The 6-min coastal sea levels (including tides) simulated and observed at the seven tide gauges with complete signals throughout September 2017 are shown in Figure 12. These are complementary to the nontidal residual plots (Figure 7) discussed earlier. The error metrics for September 2017 are shown in Figure 13, in which they are computed for both 2DDI model runs using the yearly based demeaned sea levels, and again for the 2DDI-BT model using a zero mean offset between observations for the month. This is used to help distinguish between model skill as related to capturing the monthly averaged background water level, and the model skill as related to intramonth nontidal variations that the inclusion of ocean baroclinicity may assist in capturing.

Summarizing the results of the three error metrics: the 2DDI-BC is superior at 7 (*RMSE*), 10 (γ^2), and 10 (*Skill*) tide gauges (out of 14) while the 2DDI-BT with no mean offset is better otherwise. Against the offset 2DDI-BT model, 2DDI-BC is better at 11 (*RMSE*), 10 (γ^2), and 13 (*Skill*) tide gauges. Note that the offset has no effect on γ^2. The decrease in *RMSE* for the 2DDI-BT model with no mean offset can be attributed to the decrease in *systematic* errors—the mean $RMSE_s$ is decreased from 5.6 cm (SD = 2.0 cm) to 3.9 cm

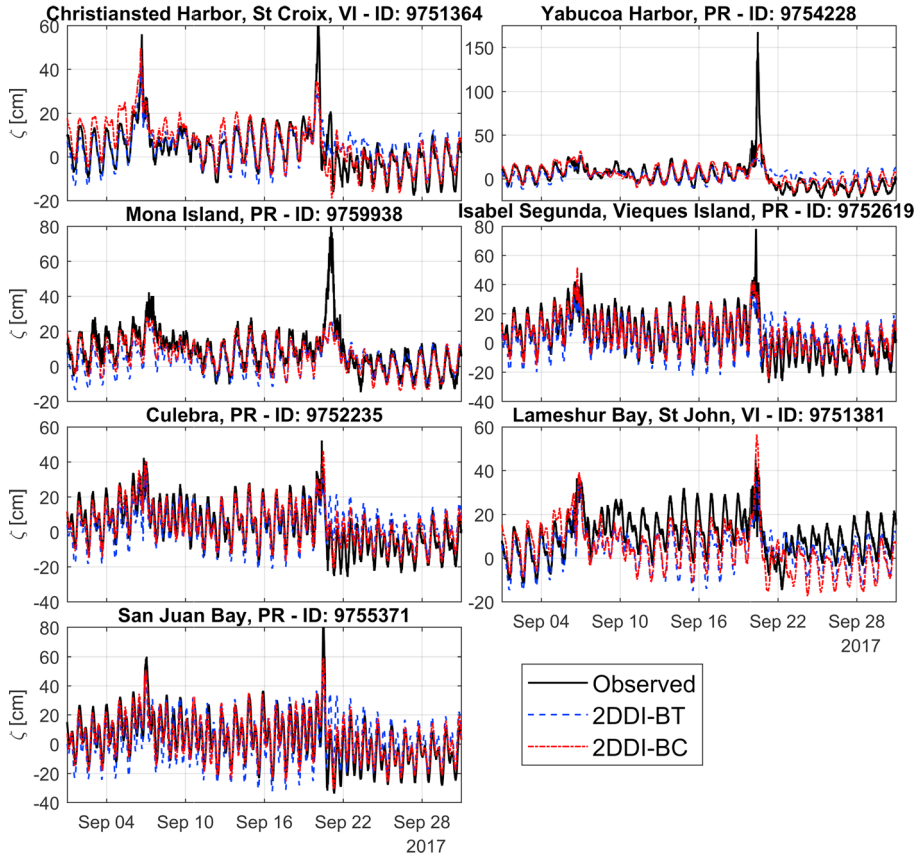

Figure 12. The 6-min coastal sea levels during September 2017 at the National Oceanic and Atmospheric Administration/National Ocean Service tide gauges (that have complete signals throughout September 2017) in the Puerto Rico and the U.S. Virgin Islands region comparing observations with the 2DDI-BT and 2DDI-BC ADvanced CIRCulation model simulations. Note that these are demeaned sea levels where the mean has been calculated independently for each time series over the year. 2DDI-BT = two-dimensional depth-integrated barotropic mode; 2DDI-BC = baroclinic-coupled 2DDI.

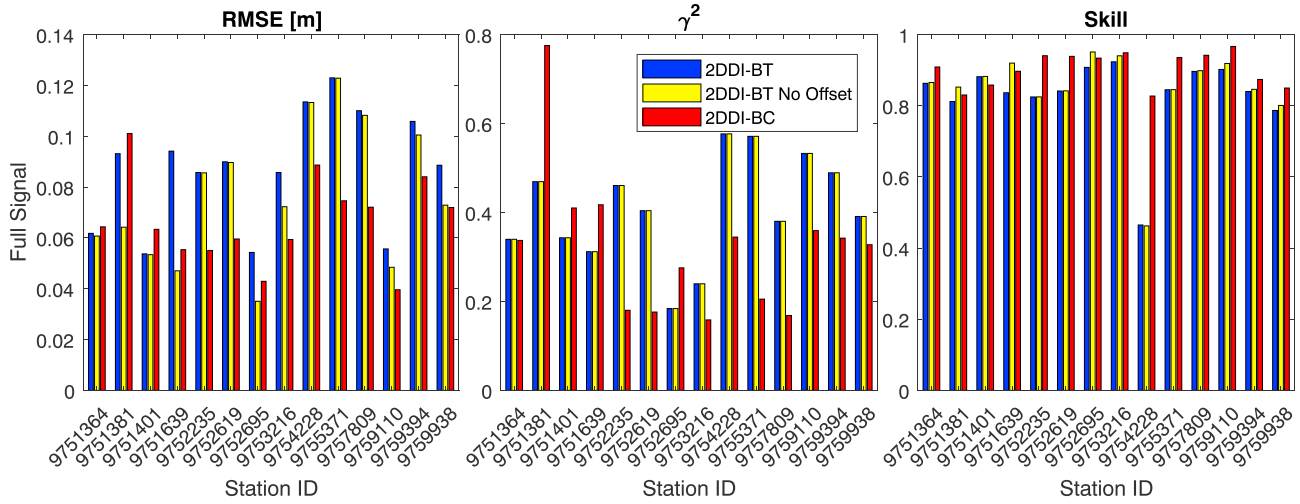

Figure 13. September 2017 error metrics—*RMSE* (left), γ^2 (middle), *Skill* (right)—for the 2DDI-BT and 2DDI-BC model simulations versus observations at the 14 National Oceanic and Atmospheric Administration/National Ocean Service tide gauges in the Puerto Rico and the U.S. Virgin Islands region. The "2DDI-BT No Offset" case computes the error with zero mean offset between observed and simulated sea levels for the month. The other two cases have nonzero mean offsets for the month based on yearly variations (see e.g., Figure 6). 2DDI-BT = two-dimensional depth-integrated barotropic mode; 2DDI-BC = baroclinic-coupled 2DDI.

(SD = 2.4 cm). In a forecast situation, the mean offset can only be estimated based on prior information measured over the previous week(s) hence the mean offset during a storm event can in general not be reduced to exactly zero. Thus, the decrease in errors (increase in *Skill*) for 2DDI-BT will be at most that shown here. Moreover, despite perfect information on the mean water level offset, the 2DDI-BC still performs best overall considering all three metrics. In fact, the mean $RMSE_s$ for the 2DDI-BC model is 3.5 cm (SD = 1.7 cm), 0.4 cm smaller than the 2DDI-BT model with no mean offset.

The 2DDI-BC performs most poorly at the four U.S. Virgin Islands tide gauges (IDs: 9751364, 9751381, 9751401, 9751639) and at Esperanza on the southern coast of Vieques Island (ID: 9752695). As indicated in Figure 6, the addition of baroclinicity does not improve the modeling of the seasonal cycle at Lameshur Bay, St. John (ID: 9751381), and the background water levels during September are around 10 cm below observations after Hurricane Irma (Figures 7 and 12). Moreover, the variance in the error (γ^2) is noticeably higher in the 2DDI-BC model at this tide gauge. This is most likely explained by a deficiency in the baroclinic structure of the GOFS 3.1 model (due to, e.g., insufficient mesh resolution) in the narrow region (≈50 km across) in between St. Croix and the main PRVI shelf where the ocean floor suddenly plummets to depths below 5,000 m.

4. Discussion and Conclusions

This study has analyzed 6-min coastal sea level variations in the PRVI region during 2017, with a special focus on September when Hurricanes Irma and Maria struck, comparing observations at 14 tide gauges with high-resolution depth-integrated (2DDI) simulations on an unstructured mesh using the ADCIRC model. The effects of accounting for ocean baroclinicity in 2DDI ADCIRC through one-way coupling with a comparatively coarse resolution operational data-assimilated 3-D baroclinic ocean model (GOFS 3.1) has been assessed. In the current setup the baroclinic coupling (2DDI-BC) requires an additional 12% of wall-clock time, compared to the barotropic only model simulation (2DDI-BT).

Our analyses indicate that the spectral density of coastal sea level variations is increased across the spectrum when ocean baroclinicity is included resulting in closer agreement to observations. This was not only apparent in the subtidal and intratidal range as would be expected, but higher energy even appeared to cascade down into the supertidal range. In this range (0.5–5 cycles per hour), shelf-resonant seiching was observed and modeled at a number of the tide gauges, which we argued to be primarily induced by the hourly meteorological forcing. The excitation of shelf modes at some of the tide gauges was only induced, or induced with higher energy, in the 2DDI-BC version of the model even though baroclinic information from GOFS 3.1 is 3-hourly. This is particularly apparent at Yabucoa Harbor (ID: 9754228) where the excitation of the fundamental shelf mode, which is also observed, only occurs in the 2DDI-BC model. A plausible explanation is that the increase in the energy throughout the spectrum in the 2DDI-BC model cascades down through to higher-frequency modes. While the supertidal response of 2DDI-BC model does appear to be more in line with observations, it is not necessarily clear that the excitation of these modes occurs through the correct physical processes or simply through the addition of noise into the system. Investigation at more coastal regions will be required to further understand this.

Baroclinically induced variations in sea levels are largely reproduced by the 2DDI-BC model. Such variations include seasonal cycles affected by the large-scale dynamics of the ocean, and other more localized impacts such as sea level setdown due to trailing cold wakes in the ocean surface temperature caused by vertical mixing from the passing hurricanes in September 2017. Where the seasonal sea level cycle was well represented the 2DDI-BC is superior to the GOFS 3.1 model indicating that it may be potentially used to downscale global 3D-BC models to the coast. Seasonal cycles were most poorly represented in the southern U.S. Virgin Islands region perhaps due to insufficient mesh resolution of the GOFS 3.1 model in the narrow steep-slopped deep ocean region between St. Croix and the main PRVI shelf. Localized sea level setdowns were noted particularly around the northeastern areas of the PRVI region following Hurricane Maria. Due to the tracking of Hurricane Irma further north of PRVI, localized setdowns were negligible in the PRVI region although were simulated around the northern Lesser Antilles.

Model performance for the entire year was improved at all tide gauges (based on the three error metrics used) when ocean baroclinicity was included. It was highlighted that baroclinicity appears to have a large impact on the reduction in systematic errors, which are most important to model fidelity. As a result, even when the

mean offset between observations and 2DDI-BT for the month of September is set to zero, 2DDI-BC (which directly simulates changes to the mean background water levels throughout the year) is superior at 10 out of the 14 tide gauges considering the γ^2 and *Skill* error metrics computed for that month. Again, the southern U.S. Virgin Islands region proved most problematic for the 2DDI-BC model. Although baroclinic coupling with the GOFS 3.1 model decreases the systematic errors, increases in the unsystematic errors of the nontidal residual were found with the implication being that additional uncertainty is inserted into the system. Even though the computational domain boundaries were extended to minimize the spurious modes originating from the lateral open boundary where the GOFS 3.1 free surface levels are prescribed, it is plausible that remnants of these modes persist contributing to the unsystematic errors. Further, data assimilation in the GOFS 3.1 model may trigger large corrections to their modeled salinity and temperature fields at times. However, when the unsystematic errors are instead computed on the full signal (including tides) they are actually smaller in 2DDI-BC than 2DDI-BT on average. In any case, the analysis of unsystematic errors and uncertainty warrants further attention in future work.

The inclusion of ocean baroclinicity with parameterized internal tide conversion increases friction in the ocean changing the location of the M_2 tidal amphidrome off the southeast coast of Puerto Rico, generally reducing tidal amplitudes, and shifting (improving) tidal phase lags in the region. Overall, ocean baroclinicity was found to decrease the mean tidal *RMSE* discrepancy at the tide gauges by 22%. However, from our experience the tidal discrepancy is smaller for the U.S. Atlantic and Gulf Coasts in general when a smaller mesh domain is used with a single lateral open boundary along the 60°W meridian. On the other hand, currently we find that the larger mesh domain with lateral open boundaries along the 22.5°S and 59.9°N parallels allows for improved large-scale response to the baroclinic forcing. Hence, we are actively working on further improvements to lateral open boundary conditions and placement (or their removal through a global model), and the distribution of internal dissipative effects to overcome this conflict.

The baroclinic-coupled 2DDI model employed in the study was shown to be capable of replicating baroclinically driven features of coastal water levels leading to improvements in the overall model skill versus the barotropic 2DDI model. These improvements could help refine flood risk warning metrics in operational forecast models particularly if coastal sea levels are close to a flood tipping point. Furthermore, while the effects of wind waves (Joyce et al., 2019) and compound flooding (Silva-Araya et al., 2018) that were not considered here are particularly critical to PRVI, both of these processes are dependent on background sea levels which have improved representation through baroclinic coupling. In future work we aim to combine wind waves and hydrological coupling effects into the analysis, and extend the 2DDI-BC model to mild-sloped wide-shelved areas such as the U.S. Atlantic and Gulf Coasts, where climatic and oceanographic variability is larger than in the Caribbean, to more thoroughly assess its capabilities and limitations.

Acknowledgments
The authors would like to thank the Southeastern Universities Research Association (SURA), awards NA13NOS0120139 (NOAA Center for Weather and Climate Prediction) and PTX-SURA-2013-008 (University of Notre Dame), NOAA's National Ocean Service and the U.S. IOOS Coastal and Ocean Modeling Testbed for supporting the work presented here. The model simulation results used in this study will be made available for download at the U.S. IOOS COMT - Puerto Rico/U.S. Virgin Islands Storm Surge project website (https://comt.ioos.us/projects/pr_inundation). The NOAA/NOS observational tide gauge data used for coastal sea level comparisons in this study are available from NOAA website (https://tidesandcurrents.noaa.gov/stations.html?type=Water+Levels). The 3-hourly GOFS 3.1 model analysis data used to drive ocean baroclinicity in the 2DDI-BC ADCIRC model are found online (http://tds.hycom.org/thredds/catalog.html).

References

Arbic, B. K., Wallcraft, A. J., & Metzger, E. J. (2010). Concurrent simulation of the eddying general circulation and tides in a global ocean model. *Ocean Modelling*, *32*(3), 175–187. https://doi.org/10.1016/j.ocemod.2010.01.007

Bacopoulos, P., Tang, Y., Wang, D., & Hagen, S. C. (2017). Integrated hydrologic-hydrodynamic modeling of estuarine-riverine flooding: 2008 Tropical Storm Fay. *Journal of Hydrologic Engineering*, *22*(8), 401722. https://doi.org/10.1061/(ASCE)HE.1943-5584.0001539

Bunya, S., Dietrich, J. C., Westerink, J. J., Ebersole, B. A., Smith, J. M., Atkinson, J. H., et al. (2010). A high-resolution coupled riverine flow, tide, wind, wind wave, and storm surge model for southern Louisiana and Mississippi. Part I: Model development and validation. *Monthly Weather Review*, *138*(2), 345–377. https://doi.org/10.1175/2009MWR2906.1

Cangialosi, J. P., Latto, A. S., & Berg, R. (2018). National huricane center tropical cyclone report - Hurricane Irma (AL112017) (Tech. Rep.): National Hurricane Center.

Carrére, L., & Lyard, F. (2003). Modeling the barotropic response of the global ocean to atmospheric wind and pressure forcing - comparisons with observations. *Geophysical Research Letters*, *30*(6), 1275. https://doi.org/10.1029/2002GL016473

Chardon-Maldonado, P., Fleming, R., & Wallinga, J. (2018). Riders on the storm - CARICOOS moored oceanographic data buoys during the 2017 hurricane season. In *OCEANS 2018*, Kobe, pp. 7.

Chassignet, E. P., Hurlburt, H. E., Smedstad, O. M., Halliwell, G. R., Hogan, P. J., Wallcraft, A. J., et al. (2007). The HYCOM (HYbrid Coordinate Ocean Model) data assimilative system. *Journal of Marine Systems*, *65*(1–4), 60–83. https://doi.org/10.1016/j.jmarsys.2005.09.016

Codiga, D. L. (2011). Unified tidal analysis and prediction using the UTide Matlab functions (Tech. Rep. 01). Narragansett, RI: Graduate School of Oceanography, University of Rhode Island. https://doi.org/10.13140/RG.2.1.3761.2008

Cummings, J. A. (2006). Operational multivariate ocean data assimilation. *Quarterly Journal of the Royal Meteorological Society*, *131*(613), 3583–3604. https://doi.org/10.1256/qj.05.105

Dietrich, J., Zijlema, M., Westerink, J., Holthuijsen, L., Dawson, C., Luettich, R., et al. (2011). Modeling hurricane waves and storm surge using integrally-coupled, scalable computations. *Coastal Engineering*, *58*(1), 45–65. https://doi.org/10.1016/j.coastaleng.2010.08.001

Dresback, K. M., Fleming, J. G., Blanton, B. O., Kaiser, C., Gourley, J. J., Tromble, E. M., et al. (2013). Skill assessment of a real-time forecast system utilizing a coupled hydrologic and coastal hydrodynamic model during Hurricane Irene (2011). *Continental Shelf Research*, *71*, 78–94. https://doi.org/10.1016/j.csr.2013.10.007

Egbert, G. D., Ray, R. D., & Bills, B. G. (2004). Numerical modeling of the global semidiurnal tide in the present day and in the last glacial maximum. *Journal of Geophysical Research*, *109*, C03003. https://doi.org/10.1029/2003JC001973

Emanuel, K. (2001). Contribution of tropical cyclones to meridional heat transport by the oceans. *Journal of Geophysical Research Atmospheres*, *106*(D14), 14771–14781. https://doi.org/10.1029/2000JD900641

Fleming, J. G., Fulcher, C. W., Luettich, R. a., Estrade, B. D., Allen, G. D., & Winer, H. S. (2008). A real time storm surge forecasting system using ADCIRC. In *10th international conference on estuarine and coastal modeling* (pp. 893–912). Rhode Island: Newport. https://doi.org/10.1061/40990(324)48

Funakoshi, Y., Feyen, J. C., Aikman, F., Tolman, H. L., van der Westhuysen, A. J., Chawla, A., et al. (2011). Development of extratropical surge and tide operational forecast system (ESTOFS), 12th International Conference on Estuarine and Coastal Modeling, St. Augustine, Florida, pp. 201–212.

Garratt, J. R. (1977). Review of drag coefficients over oceans and continents. *Monthly Weather Review*, *105*(7), 915–929. https://doi.org/10.1175/1520-0493(1977)105<0915:RODCOO>2.0.CO;2

Giese, G. S., Chapman, D. C., Black, P. G., & Fornshell, J. A. (1990). Causation of large-amplitude coastal seiches on the Caribbean coast of Puerto Rico. *Journal of Physical Oceanography*, *20*(9), 1449–1458. https://doi.org/10.1175/1520-0485(1990)020<1449:COLACS>2.0.CO;2

Green, J. A. M., & Nycander, J. (2013). A comparison of tidal conversion parameterizations for tidal models. *Journal of Physical Oceanography*, *43*(1), 104–119. https://doi.org/10.1175/JPO-D-12-023.1

Hope, M. E., Westerink, J. J., Kennedy, A. B., Kerr, P. C., Dietrich, J. C., Dawson, C., et al. (2013). Hindcast and validation of Hurricane Ike (2008) waves, forerunner, and storm surge. *Journal of Geophysical Research: Oceans*, *118*, 4424–4460. https://doi.org/10.1002/jgrc.20314

Joyce, B., Gonzalez-Lopez, J., van der Westhuysen, A. J., Yang, D., Pringle, W. J., Westerink, J. J., & Cox, A. T. (2019). U.S. IOOS coastal and ocean modeling testbed: Hurricane-induced waves, surge, and inundation for deep-ocean, reef-fringed islands in the Caribbean. *Journal of Geophysical Research: Oceans*, https://doi.org/10.1029/2018JC01468

Kennedy, A. B., Westerink, J. J., Smith, J. M., Hope, M. E., Hartman, M., Taflanidis, A. A., et al. (2012). Tropical cyclone inundation potential on the Hawaiian Islands of Oahu and Kauai. *Ocean Modelling*, *52-53*, 54–68. https://doi.org/10.1016/j.ocemod.2012.04.009

Kerr, P. C., Donahue, A. S., Westerink, J. J., Luettich, R. A., Zheng, L. Y., Weisberg, R. H., et al. (2013). U.S. IOOS coastal and ocean modeling testbed: Inter-model evaluation of tides, waves, and hurricane surge in the Gulf of Mexico. *Journal of Geophysical Research: Oceans*, *118*, 5129–5172. https://doi.org/10.1002/jgrc.20376

Kerr, P. C., Martyr, R. C., Donahue, A. S., Hope, M. E., Westerink, J. J., Luettich, R. A., et al. (2013). U.S. IOOS coastal and ocean modeling testbed: Evaluation of tide, wave, and hurricane surge response sensitivities to mesh resolution and friction in the Gulf of Mexico. *Journal of Geophysical Research: Oceans*, *118*, 4633–4661. https://doi.org/10.1002/jgrc.20305

Kjerfve, B. (1981). Tides of the Caribbean Sea. *Journal of Geophysical Research*, *86*(C5), 4243–4247. https://doi.org/10.1029/JC086iC05p04243

Kodaira, T., Thompson, K. R., & Bernier, N. B. (2016). The effect of density stratification on the prediction of global storm surges. *Ocean Dynamics*, *66*(12), 1733–1743. https://doi.org/10.1007/s10236-016-1003-6

Luettich, R. A., & Westerink, J. J. (2004). Formulation and numerical implementation of the 2D/3D ADCIRC finite element model version 44.XX (*Tech. rep.*). Morehead City, NC: University of North Carolina at Chapel Hill, Notre Dame, IN: University of Notre Dame.

Luettich, R. A., Wright, L. D., Nichols, C. R., Baltes, R., Friedrichs, M. A. M., Kurapov, A., et al. (2017). A test bed for coastal and ocean modeling. *Eos*, *98*. https://doi.org/10.1029/2017EO078243

McDougall, T. J., & Barker, P. M. (2011). Getting started with TEOS-10 and the Gibbs Seawater (GSW) oceanographic toolbox. 28 pp., SCOR/IAPSO WG127.

Melet, A., Meyssignac, B., Almar, R., & Le Cozannet, G. (2018). Under-estimated wave contribution to coastal sea-level rise. *Nature Climate Change*, *8*(3), 234–239. https://doi.org/10.1038/s41558-018-0088-y

Metzger, E. J., Helber, R., Hogan, P. J., Posey, P. G., Thoppil, P. G., Townsend, T. L., et al. (2017). Global ocean forecast system 3.1 validation testing (Tech. Rep.): Naval Research Laboratory, Stennis Space Center, MS 39529-5004.

Orton, P., Georgas, N., Blumberg, A., & Pullen, J. (2012). Detailed modeling of recent severe storm tides in estuaries of the New York City region. *Journal of Geophysical Research*, *117*, 1–17. https://doi.org/10.1029/2012JC008220

Pasch, R. J., Penny, A. B., & Berg, V (2018). National huricane center tropical cyclone report - Hurricane Maria (AL152017) (Tech. Rep.): National Hurricane Center.

Pringle, W. J., Wirasaet, D., Suhardjo, A., Meixner, J., Westerink, J. J., Kennedy, A. B., & Nong, S. (2018). Finite-element barotropic model for the Indian and Western Pacific Oceans: Tidal model-data comparisons and sensitivities. *Ocean Modelling*, *129*, 13–38. https://doi.org/10.1016/j.ocemod.2018.07.003

Pringle, W. J., Wirasaet, D., & Westerink, J. J. (2018). Modifications to internal tide conversion parameterizations and implementation into barotropic ocean models. *EarthArXiv*, 9. https://doi.org/10.31223/osf.io/84w53

Resio, D. T., & Westerink, J. J. (2008). Modeling the physics of storm surges. *Physics Today*, *61*(9), 33–38. https://doi.org/10.1063/1.2982120

Roberts, K. J., Pringle, W. J., & Westerink, J. J. (2018). OceanMesh2D 1.0: MATLAB-based software for two-dimensional unstructured mesh generation in coastal ocean modeling. *Geoscientific Model Development Discussions*, *36*. https://doi.org/10.5194/gmd-2018-203

Saha, S., Moorthi, S., Wu, X., Wang, J., Nadiga, S., Tripp, P., et al. (2014). The NCEP climate forecast system version 2. *Journal of Climate*, *27*(6), 2185–2208. https://doi.org/10.1175/JCLI-D-12-00823.1

Savage, A. C., Arbic, B. K., Richman, J. G., Shriver, J. F., Alford, M. H., Buijsman, M. C., et al. (2017). Frequency content of sea surface height variability from internal gravity waves to mesoscale eddies. *Journal of Geophysical Research: Oceans*, *122*, 2519–2538. https://doi.org/10.1002/2016JC012331

Shchepetkin, A. F., & McWilliams, J. C. (2005). The regional oceanic modeling system (ROMS): A split-explicit, free-surface, topography-following-coordinate oceanic model. *Ocean Modelling*, *9*(4), 347–404. https://doi.org/10.1016/j.ocemod.2004.08.002

Silva-Araya, W., Santiago-Collazo, F., Gonzalez-Lopez, J., & Maldonado-Maldonado, J. (2018). Dynamic modeling of surface runoff and storm surge during hurricane and tropical storm events. *Hydrology*, *5*(1), 13. https://doi.org/10.3390/hydrology5010013

Smagorinsky, J. (1963). General circulation experiments with the primitive equations. I. The basic experiment. *Monthly Weather Review*, *91*(3), 99–164. https://doi.org/10.1175/1520-0493(1963)091<0099:GCEWTP>2.3.CO;2

Tanaka, S., Bunya, S., Westerink, J. J., Dawson, C., & Luettich, R. A. (2011). Scalability of an unstructured grid continuous Galerkin based hurricane storm surge model. *Journal of Scientific Computing*, *46*(3), 329–358. https://doi.org/10.1007/s10915-010-9402-1

Technology Riverside Inc, & AECOM (2015). Mesh development, tidal validation, and hindcast skill assessment of an ADCIRC model for the hurricane storm surge operational forecast system on the US Gulf-Atlantic coast (Tech. Rep.): National Oceanic and Atmospheric Administration/Nation Ocean Service, Coast Survey Development Laboratory, Office of Coast Survey. https://doi.org/10.7921/G0MC8x6V

Thomson, D. J. (1982). Spectrum estimation and harmonic analysis. *Proceedings of the IEEE*, *70*(9), 1055–1096. https://doi.org/10.1109/PROC.1982.12433

Torres, R. R., & Tsimplis, M. N. (2012). Seasonal sea level cycle in the Caribbean Sea. *Journal of Geophysical Research*, *117*, 1–18. https://doi.org/10.1029/2012JC008159

Van Cooten, S., Kelleher, K. E., Howard, K., Zhang, J., Gourley, J. J., Kain, J. S., et al. (2011). The CI-flow project: A system for total water level prediction from the summit to the sea. *Bulletin of the American Meteorological Society*, *92*(11), 1427–1442. https://doi.org/10.1175/2011BAMS3150.1

Vinogradov, S. V., Myers, E., Funakoshi, Y., & Kuang, L. (2017). Development and validation of operational storm surge model guidance. In *15th Symposium on the Coastal Environment at the 97th AMS Annual Meeting*, Seattle, Washington.

Wessel, P., & Smith, W. H. F. (1996). A global, self-consistent, hierarchical, high-resolution shoreline database. *Journal of Geophysical Research*, *101*(B4), 8741–8743. https://doi.org/10.1029/96JB00104

Westerink, J. J., Luettich, R. A., Feyen, J. C., Atkinson, J. H., Dawson, C., Roberts, H. J., et al. (2008). A basin- to channel-scale unstructured grid hurricane storm surge model applied to southern Louisiana. *Monthly Weather Review*, *136*(3), 833–864. https://doi.org/10.1175/2007MWR1946.1

Willmott, C. J. (1981). On the validation of models. *Physical Geography*, *2*(2), 184–194. https://doi.org/10.1080/02723646.1981.10642213

Wilmes, S. B., Green, J. A., Gomez, N., Rippeth, T. P., & Lau, H. (2017). Global tidal impacts of large-scale ice sheet collapses. *Journal of Geophysical Research: Oceans*, *122*, 8354–8370. https://doi.org/10.1002/2017JC013109

Zheng, L., Weisberg, R. H., Huang, Y., Luettich, R. A., Westerink, J. J., Kerr, P. C., et al. (2013). Implications from the comparisons between two- and three- dimensional model simulations of the Hurricane Ike storm surge. *Journal of Geophysical Research: Oceans*, *118*, 3350–3369. https://doi.org/10.1002/jgrc.20248